Lehigh University
Lehigh Preserve

Theses and Dissertations

1991

A statistical analysis of reliability for vapor grown planar InGaAs/InP photodiodes

Mark M. Marvi
Lehigh University

Follow this and additional works at: https://preserve.lehigh.edu/etd

Part of the Electrical and Computer Engineering Commons

Recommended Citation
Marvi, Mark M., "A statistical analysis of reliability for vapor grown planar InGaAs/InP photodiodes" (1991). *Theses and Dissertations*. 5386.
https://preserve.lehigh.edu/etd/5386

This Thesis is brought to you for free and open access by Lehigh Preserve. It has been accepted for inclusion in Theses and Dissertations by an authorized administrator of Lehigh Preserve. For more information, please contact preserve@lehigh.edu.

A STATISTICAL ANALYSIS OF RELIABILITY FOR VAPOR GROWN PLANAR InGaAs/InP PHOTODIODES

by

Mark M. Marvi

A Thesis

Presented to the Graduate Committee

of Lehigh University

in Candidacy for the Degree of

Master of Science

in

Electrical Engineering

Lehigh University

1990

This Thesis is accepted and approved in partial fulfillment of the requirements for the degree of Master of Science in Electrical Engineering.

September 19, 1990

(date)

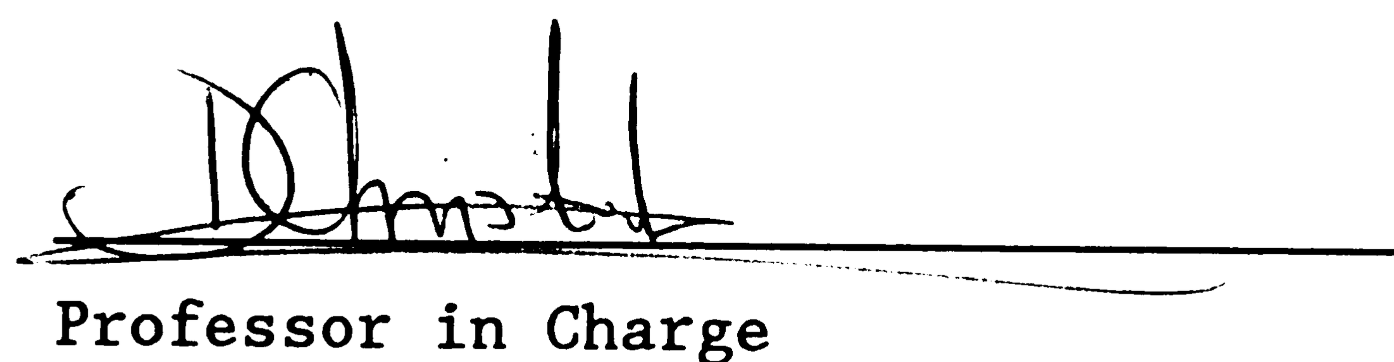

Professor in Charge

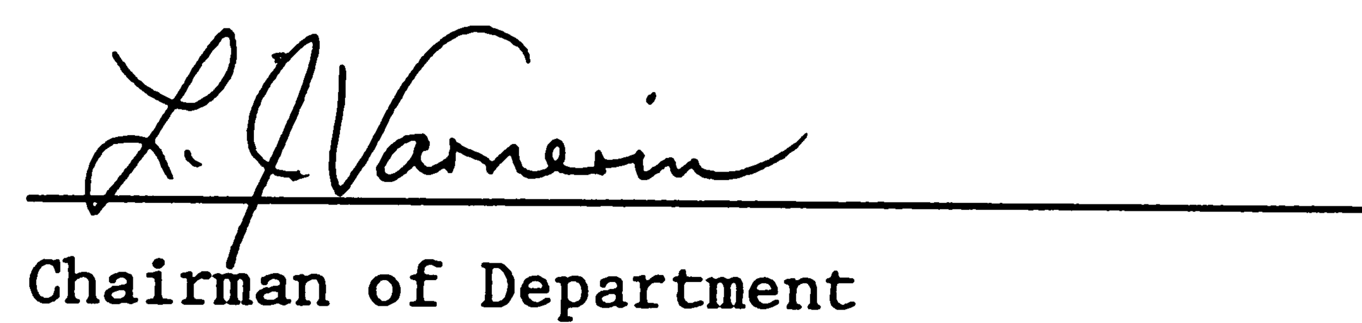

Chairman of Department

TABLE OF CONTENTS

ABSTRACT	pg 1
INTRODUCTION	pg 2
ACCELERATION METHODS	pg 4
RELIABILITY CONCEPTS	pg 9
DEVICE FABRICATION	pg 24
SYSTEM REQUIREMENTS	pg 38
EXPERIMENT OUTLINE	pg 41
RESULTS	pg 46
CONCLUSIONS	pg 82
REFERENCES AND BIBLIOGRAPHY	pg 83
VITA	pg 86

LIST OF TABLES

Table 1.	Values of chi-squared	pg 22
Table 2.	AT&T long wavelength pin photodiode performance	pg 27
Table 3.	200 Degree Celsius Matrix	pg 42
Table 4.	250 Degree Celsius Matrix	pg 42
Table 5.	Burn-In Failures	pg 47
Table 6.	250 Degree Celsius Aging Failures	pg 61
Table 7.	Predicted Random Failure Rates	pg 73
Table 8.	200 Degree Celsius Aging Failure FMAs	pg 79
Table 9.	250 Degree Celsius Aging Failure FMAs	pg 80

LIST OF FIGURES

Figure 1.	Reliability Bathtub Curve	pg 11
Figure 2.	Weibull Cumulative Failure Plot	pg 14
Figure 3.	Weibull Plot	pg 18
Figure 4.	Cumulative Failure, F_{MTTF}, Plot	pg 20
Figure 5.	Structure of AT&T pin photodiode	pg 25
Figure 6.	Typical I-V Curve for InGaAs pin Photodetector	pg 26
Figure 7.	Typical I-V, dI/dV Trace	pg 31
Figure 8.	Typical Low Noise dI/dV Trace	pg 33
Figure 9.	Typical Mid Noise dI/dV Trace	pg 34
Figure 10.	Typical High Noise dI/dV Trace	pg 35
Figure 11.	Device #56 @ t=0 Hours	pg 48
Figure 12.	Device #56 @ t=1326 Hours	pg 49
Figure 13.	Device #56 @ t=2307 Hours	pg 50
Figure 14a	Dark Current for 76 μm Diameter Junction Device @ 200 Degree Celsius, High dI/dV Noise	pg 52

Figure 14b	Dark Current for 76 µm Diameter Junction Device @ 200 Degree Celsius, Mid dI/dV Noise	pg 53
Figure 14c	Dark Current for 76 µm Diameter Junction Device @ 200 Degree Celsius, Low dI/dV Noise	pg 54
Figure 15a	Dark Current for 254 µm Diameter Junction Device @ 200 Degree Celsius, High dI/dV Noise	pg 55
Figure 15b	Dark Current for 254 µm Diameter Junction Device @ 200 Degree Celsius, Mid dI/dV Noise	pg 56
Figure 15c	Dark Current for 254 µm Diameter Junction Device @ 200 Degree Celsius, Low dI/dV Noise	pg 57
Figure 16a	Dark Current for 381 µm Diameter Junction Device @ 200 Degree Celsius, High dI/dV Noise	pg 58
Figure 16b	Dark Current for 381 µm Diameter Junction Device @ 200 Degree Celsius, High I-V Ratio, Low dI/dV Noise	pg 59
Figure 16c	Dark Current for 381 µm Diameter Junction Device @ 200 Degree Celsius, Low dI/dV Noise	pg 60
Figure 17a	Dark Current for 76 µm Diameter Junction Device @ 250 Degree Celsius, High dI/dV Noise	pg 62

Figure 17b	Dark Current for 76 μm Diameter Junction Device @ 250 Degree Celsius, Mid dI/dV Noise	pg 63
Figure 17c	Dark Current for 76 μm Diameter Junction Device @ 250 Degree Celsius, Low dI/dV Noise	pg 64
Figure 18a	Dark Current for 254 μm Diameter Junction Device @ 250 Degree Celsius, High dI/dV Noise	pg 65
Figure 18b	Dark Current for 254 μm Diameter Junction Device @ 250 Degree Celsius, Mid dI/dV Noise	pg 66
Figure 18c	Dark Current for 254 μm Diameter Junction Device @ 250 Degree Celsius, Low dI/dV Noise	pg 67
Figure 19a	Dark Current for 381 μm Diameter Junction Device @ 250 Degree Celsius, High dI/dV Noise	pg 68
Figure 19b	Dark Current for 381 μm Diameter Junction Device @ 250 Degree Celsius, High I-V Ratio, Low dI/dV Noise	pg 69
Figure 19c	Dark Current for 381 μm Diameter Junction Device @ 250 Degree Celsius, Low dI/dV Noise	pg 70
Figure 20.	Cumulative Failure Plot	pg 72

Figure 21.	SEM schematic using EBIC signal technique	pg 74
Figure 22.	EBIC image of p-contact for a planar pin photodiode	pg 76
Figure 23.	Secondary Image of localized ESD damage	pg 78
Figure 24.	EBIC and Secondary Image of Device #541	pg 81

ABSTRACT

This thesis will calculate the predicted reliability of InGaAs/InP PIN photodetectors manufactured at AT&T. Current aging techniques from various published works are reviewed. A thermal aging process was used based on the device material and associated aging phenomena. Different statistical methods are evaluated for use in reliability calculations and based on accuracy, selected for reliability estimations. The impact of service life failures on system performance was the vehicle for establishing aging failure criteria. Data was collected during accelerated aging (in excess of 4300 hours at 200 Degrees Celsius) in order to determine parameters such as mean-time-to-failure (MTTF), wear-out failure rate, and random failure rate. A noise measurement, believed to be capable of predicting device reliability, exhibited no correlation to infant, random or wear out failure rates. The photodetectors were found to have a failure rate of less than .43 Failures In Time (FITs) at 20 ^{o}C service temperature and a MTTF in excess of 10^{13} hours ($>10^{9}$ years).

INTRODUCTION

At the heart of fiber optic systems are the components which convey high speed data. These components employ semiconductor lasers for the so-called long-haul transmission and light emitting diodes (LEDs) for short-haul transmission. In both transmission systems, a photodiode is used as an optical to electrical signal converter in the receiver. For semiconductor laser based systems the photodiode is also used as an optical monitor to provide feedback to the laser current driver circuitry in order to maintain a stable light output.

Fiber optic systems are superior in performance in terms of bandwidth, electromagnetic interference (EMI) immunity, cross talk reduction, and security when compared to copper based or satellite systems. However, to be cost effective in both terrestrial and submarine cable applications longer repeaterless spans are used, in excess of 60 km for long-haul and 2-3 km for short-haul. Reliability of these fiber optic components as in any system becomes a crucial variable to consider [7,8].

The first section of this thesis will address the various accelerated aging methods that can be employed to simulate and determine device reliability. Next, different reliability statistical methods will be evaluated. In each method of reliability calculation, there are inherent uncertainties which lead to calculations that are optimistically or pessimistically weighted. The third section describes the device

structure of PIN photodiodes currently manufactured at AT&T Microelectronics as well as typical device performance. The system requirements which demand a certain reliability of the photodiode are reviewed and in turn the impact of the device reliability on system performance. The fifth section will detail the experimental set-up and procedures performed. Finally, the sixth section will discuss experimental results and conclusions based on those results.

ACCELERATION METHODS

There are several methods of accelerated aging that have been used to attempt to simulate device lifetimes on the order of 10-20 years. The key is to simulate device life without subjecting the device to abnormal operating conditions that would not be experienced during its normal service life.

The most common practice, the one used in this study, of accelerated aging is to operate the PIN photodetector at the normal operating bias, 5-10 Volts, and at elevated temperatures 120-300 ^{o}C [11],[12],[15]. This method is referred to as a thermal overstress. Other methods are similar but include additional overstresses such as: biasing the photodetector above the operating bias (bias overstress) and/or increasing the humidity from a typical ambient humidity of 20-30% to 50-85% (humidity overstress) [7].

The problem with these overstress conditions, bias and humidity, is that they tend to introduce new failure modes which are not commonly seen during device lifetime [1],[2],[7],[12],[15],[16]. The exclusion of bias and humidity overstressing is based on the assumption that the photodetectors operate in an environment free from such abnormal operating conditions.

When using thermal overstressing, the effects of temperature must be understood. The work performed by British Telecom Research Laboratories, [1], indicates that accelerated aging at temperatures exceeding 300 ^{o}C causes InP based devices to degrade unnaturally. On the other hand, if temperatures less than 120 degrees Celsius are used, the aging time starts to approach service life time and becomes impractical for gathering experimental data in a reasonable amount of time.

The use of thermal overstress assumes that the failure modes observed throughout service life are thermally activated. Therefore accelerated aging should enhance these failure modes. The relationship between the thermal overstress and the time to failure is derived by the activation energy of the failure mechanism which dominates the photodetector.

The activation energy is determined by applying the stress, thermal in this case, to a sample of devices over various temperature ranges and analyzing the associated failure mechanisms. Using the calculated activation energy, the acceleration factor can be determined.

The acceleration factor associated with thermal overstressing is as follows:

$$A = \frac{\text{equivalent time in service at temp } T_1}{\text{time on life test at temp } T_2} \qquad (1)$$

The Arrhenius relationship of A is given by the following expression:

$$R = R_o \exp\left[\frac{-E_A}{kT}\right] \qquad (2)$$

where R is the reaction rate of the failure mechanisms and

R_o = a constant

E_A = activation energy, (eV)

k = Boltzman constant, (8.6×10^{-5} eV/^oK)

T = absolute temperature, (^oK)

Since time to failure is inversely proportional to the reaction rate, R, the time to failure, t_f, is

$$t_f \propto \frac{1}{R} \propto \exp\left[\frac{E_A}{kT}\right] \qquad (3)$$

and

$$\ln(t_f) = C + \frac{E_A}{kT} \tag{4}$$

using EQ(2) and the temperature relationship in EQ(1), the acceleration factor, A, is derived as follows:

$$A = \frac{R_1(T_1)}{R_2(T_2)} = \exp\left[\frac{E_A}{k}\left[\frac{1}{T_1} - \frac{1}{T_2}\right]\right] \tag{5}$$

where T_1 is the worst case , highest, operating temperature of the photodetector over the service life and T_2 is the temperature of the accelerated aging of the photodetectors.

The activation energy, E_A, can be determined as stated earlier from carrying out high temperature life tests at different temperatures. The time at which some percentage (ex: $t_{50\%}$) of failures occur, determined from cumulative failure plots for each temperature, is then collected [14],[15]. A plot of $\ln(t_{50\%})$ vs 1/T, [14],[15], yields a slope of E_A/k from which E_A is calculated.

Activation energies for InGaAs based pin photodetectors have been estimated ranging from .3 to 1.6 eV [1],[7],[14]. Previous data generated by the designer's for AT&T InGaAsP pin photodetectors with a ternary structure grown by liquid phase epitaxy (LPE) estimate a worst case activation energy of .6 eV and 1.1 eV typical.

Device defects, the root cause of failures which occur prior to wear-out during the service life, have an associated activation energy. The activation energy is the amount of energy required to "enhance" the defect site. The "enhanced" defect becomes an area of high electric field or current density which causes material breakdown to occur. As a result, the device experiences a "shorting" from the anode to the cathode.

The activation energy necessary to start the run-away condition described above can be achieved either electrically (increased bias) or thermally (increased temperature). The process of photon absorption and electron-hole generation-recombination in photodiode operation occurs in such a manner that the stoichiometry of the device remains constant; therefore, chemical activation is not entertained. As mentioned earlier, the additional stress created by an increased bias may enhance the failure modes caused by defect centers. However, additional failure modes, such as early wear out due to higher electric fields, could occur and can not be distinguished from true defect related failures normally seen during device service life. Thermal activation is the only known method of activating the defect centers and hence "normal" failure modes

without subjecting the defect free areas of the photodetector to undue stress while under bias. In addition, the acceleration factor of thermal stressing is understood and agrees with the $1/kT$ factor used throughout device physics. Currently, there is no well understood relationship between increased voltage and acceleration factor which exists in the science of device physics today.

The basic premise of this study is that any failure modes that would be observed during the operational service life of a vapor phase epitaxy (VPE) grown InGaAs binary structure photodiode are thermally activated. Furthermore, these failure modes could be reproduced through long term aging at elevated temperatures.

All of the technical literature referenced in this study support the thermal activation of failure modes present in devices of similar materials, particularly the work performed by Chin et al. [14].

RELIABILITY CONCEPTS

As time frames from device concept to manufacture become increasingly shorter, the ability to predict how that device performs a function under stated conditions over time in the field becomes equally difficult. Through the use of statistical methods one is able to model the lifetime of a device which is far more practical than actually

waiting for real time data on the order of 5 to 25 years. This type of approach is widely used in calculating a system failure rate and ultimately a required failure rate for system components. There is an economical trade-off between using screens to "catch" early failures and using statistical methods to predict lifetimes which are a function of the device design [1-20].

This section will address some of the more widely used reliability calculation methods as well as the inherent advantages and disadvantages of each. The terminology used to define device lifetime differs from company to company and how they fit into the scheme of ultimately defining system reliability.

A basic principle used to describe different phases of device lifetime for a given population of manufactured product is the "bathtub" curve, see figure 1. This model describes the different failure rates of a population of devices which perform functionally but have not seen any screening with regard to reliability. As can be seen in figure 1, there are basically three regimes which categorize this population namely; infant mortality (early) failure rate, steady state (random) failure rate, and wear out failure rate.

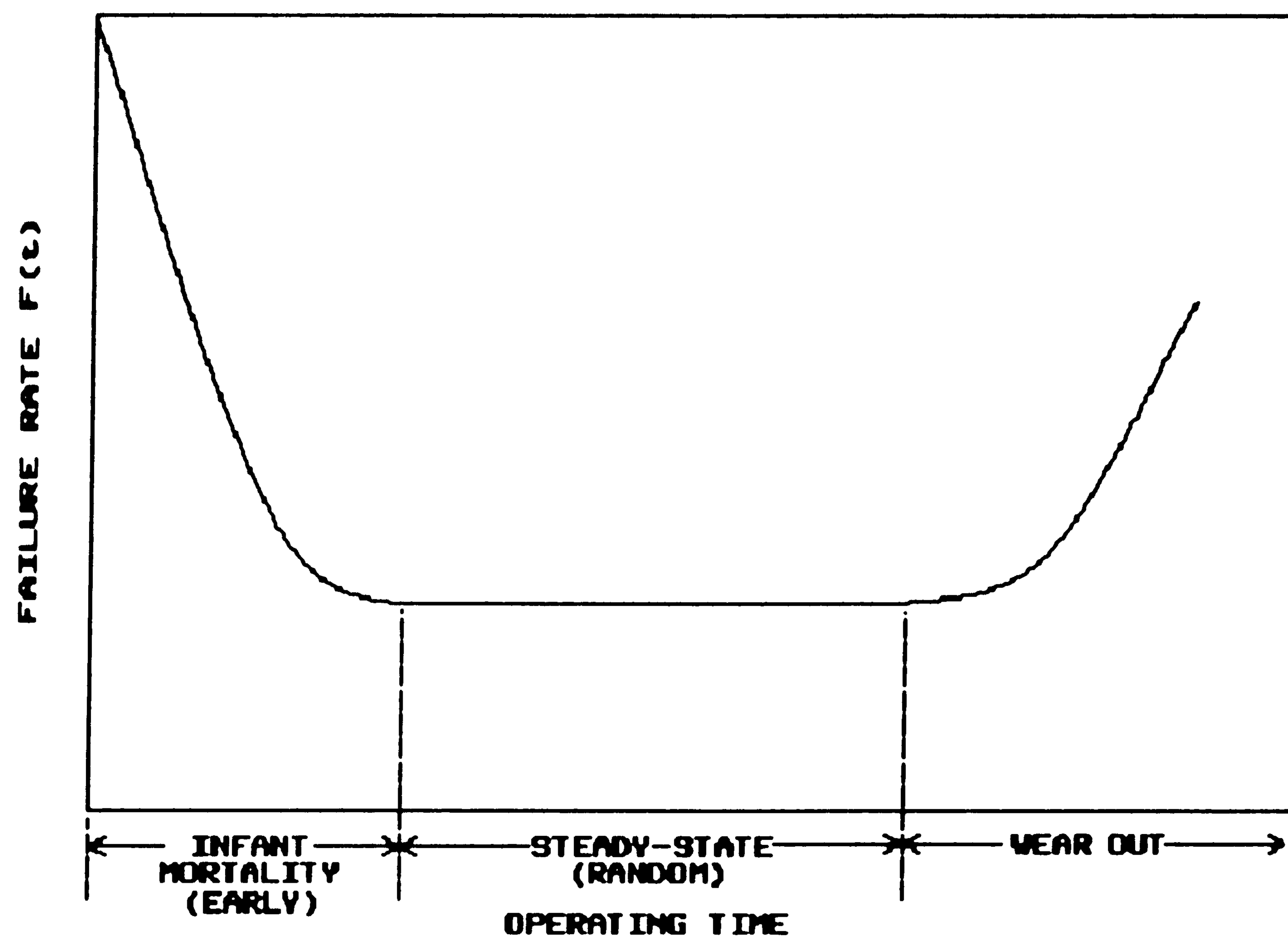

Figure 1. Reliability Bathtub Curve

The bathtub curve can be represented as either a cumulative percent of failures over time or failure rate over time:

$$F(t) = 1 - R(t) \qquad |F(t)| < 1, R(t) < 1 \qquad (6)$$

where $F(t)$ is the cumulative distribution function, the fraction of components that have failed at time t and $R(t)$ is the reliability function, the fraction of components that are surviving at time t.

The infant mortality or instantaneous failure rate is characterized by those devices which have weaknesses that are a result of interacting process variations or mistakes made when deviating from the intended

device fabrication. The infant mortality failure rate is easier to characterize due to the shorter time span of failure occurrence. In order to catch early failures all devices are subjected to stressed conditions over and above normal operating conditions i.e. thermal/mechanical cycling, high temperature high bias (HTHB) burn-in etc., which enhance device weakness and cause device failure outside of expected device performance. It is not the intention of this study to address this failure rate. These infant failures were removed from the experimental population with the use of a HTHB burn-in at a temperature of 200 ^{o}C for 5.5 hours at a reverse bias of 30 Volts. Burn-in failures are those devices which experience a dark current shift of more than ±5 nA at an operating bias of 5 Volts after the burn-in cycle is completed. As can be seen from the data presented later on, the burn-in is successful in removing infant failures.

The more challenging topic of interest and the focus of this study is understanding the last two regimes of the bathtub curve for the PIN photodiode, predicting random and wear out failure rates.

The steady-state or random failure rate as it is commonly referred is the failure rate of a device during its service life. If the failures during this period of time occur in a truly random fashion then the ability to "screen" these out becomes a formidable task such that developed life tests will show a low and possibly zero failure rate. If the screen for infant failures is adequate the random failures should

dominate the failure rate during the service life. Calculations of the random failure rate will be presented later.

The wear out failure rate represents the point in time in which the device performance starts to degrade and proceeds with a monotonically increasing failure rate. A useful analogy for wear out failure of electronic components is in machinery in which tooling physically wears with continual usage over time. The intention with machinery is to replace tooling before producing out of spec material. However, in most cases the bath-tub model falls short for electrical devices since wear out failures tend to not to degrade gradually but catastrophically to the point of causing system failure. Therefore in electrical, non-mechanical, device design it is advantageous to achieve wear out failure rates which exceed system lifetime requirements.

Distributions

There are three ways to express the distribution of cumulative failures over time. For a Weibull distribution, the reliability function $R(t)$ is calculated as follows:

$$R(t) = \exp\left[-\left[\frac{t - \delta}{\eta}\right]^{\beta}\right] \qquad (7)$$

where ß is the shape parameter determined from the slope of the plot, η is a scaling parameter and t is the time at which 63.2% of the total population has failed. δ is a location parameter which is usually zero. All parameters are constant and can be obtained from the cumulative failure plot of life test data for a population of devices as shown in figure 2.

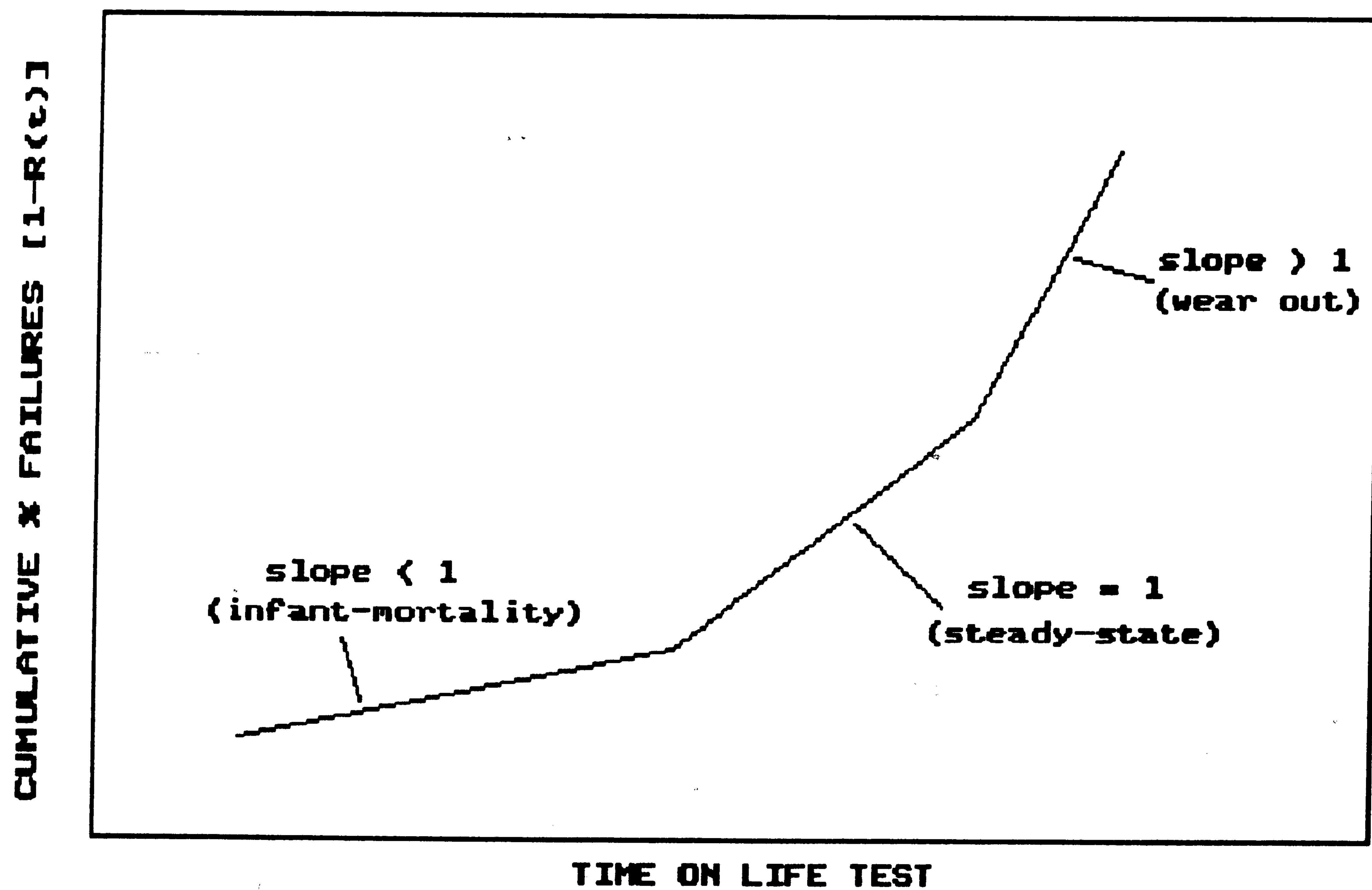

Figure 2. Weibull Cumulative Failure Plot

For a lognormal distribution the reliability function $R(t)$ is calculated as follows:

$$R(t) = 1 - \frac{1}{\sigma\sqrt{2\pi}} \int_0^t \frac{1}{t} \exp\left[-\frac{1}{2} \left[\frac{\ln(t) - \mu}{\sigma} \right]^2 \right] dt \quad (8)$$

where μ and σ are constants obtained from the cumulative failure plot of life test data using lognormal paper.

Both of these type of distribution functions characterize the cumulative distribution of failures. However, the Weibull distribution has some advantages in that the associated mathematical analysis is simple, the ß parameter of a Weibull plot indicates whether the failure rate is increasing or decreasing (because of its dependency on the slope), and tends to be more conservative in the distribution fitting and extrapolation of life test data. The mathematics for the different distributions will be presented; however, for the aforementioned reasons, the Weibull distribution will be used for all reliability calculations in this study.

For the exponential distribution the probability function is of the form

$$f(t) = \lambda e^{-\lambda t} \quad (t \geq 0) \tag{9}$$

the cumulative distribution function $F(t)$ is

$$F(t) = \int_0^t f(x)\,dx = 1 - e^{-\lambda t} \tag{10}$$

the reliability function $R(t)$ is

$$R(t) = 1 - F(t) = e^{-\lambda t} \tag{11}$$

the failure rate $\lambda(t)$ is

$$\lambda(t) = \frac{f(t)}{R(t)} = \lambda \tag{12}$$

The exponential distribution is useful in describing the random failure rate if it is constant.

The Weibull and lognormal distributions have been used in similar work by British Telecom Research Laboratories, [1] and the lognormal distribution used by others [13],[15].

MTTF,MTBF,FIT Rates

Some of the terminology used to describe device lifetime exists in the form of; Mean-Time-To-Failure (MTTF) rate, Mean-Time-Between-Failure (MTBF) rate, and the Failure-In-Time (FIT) rate.

The MTTF rate is the average predicted time to failure and is derived as follows:

$$MTTF = \int_0^{\infty} f(x)\,dx \qquad (13)$$

for a Weibull distribution, it is expressed as follows

$$\text{MTTF} = \left[\Gamma \left(1 + \frac{1}{\beta} \right) \right] \eta \qquad (14)$$

using the Gamma Function where $\Gamma(N) = (N-1)!$ one can generate MTTF/η vs ß as in figure 3.

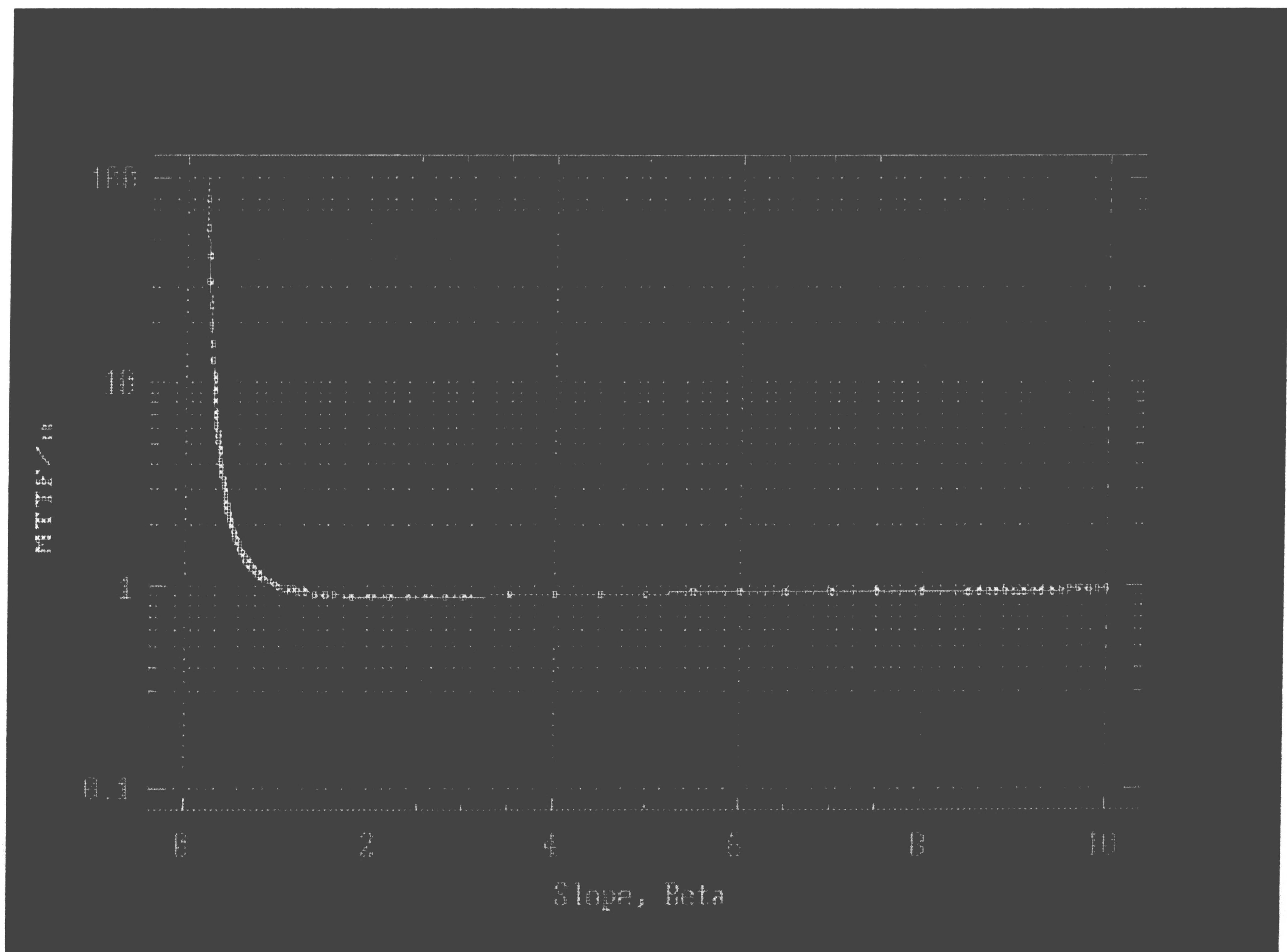

Figure 3. Weibull Plot

Using equations (6) & (7), $F(t)$ can also be plotted, see Figure 4.

The MTTF can be calculated with a lognormal distribution similarly using the σ and μ parameters. Using the exponential distribution MTTF is expressed as

$$\text{MTTF} = \int_0^\infty \lambda t e^{-\lambda t}\, dt = \frac{1}{\lambda} \tag{15}$$

since the failure rate is constant when using an exponential distribution, then the MTBF is also constant yielding

$$\text{MTTF} = \text{MTBF} = \frac{1}{\lambda} \tag{16}$$

MTTF is useful in describing the failure rate of electronic devices when the failure rate is constant as during the service life if the failures are truly random.

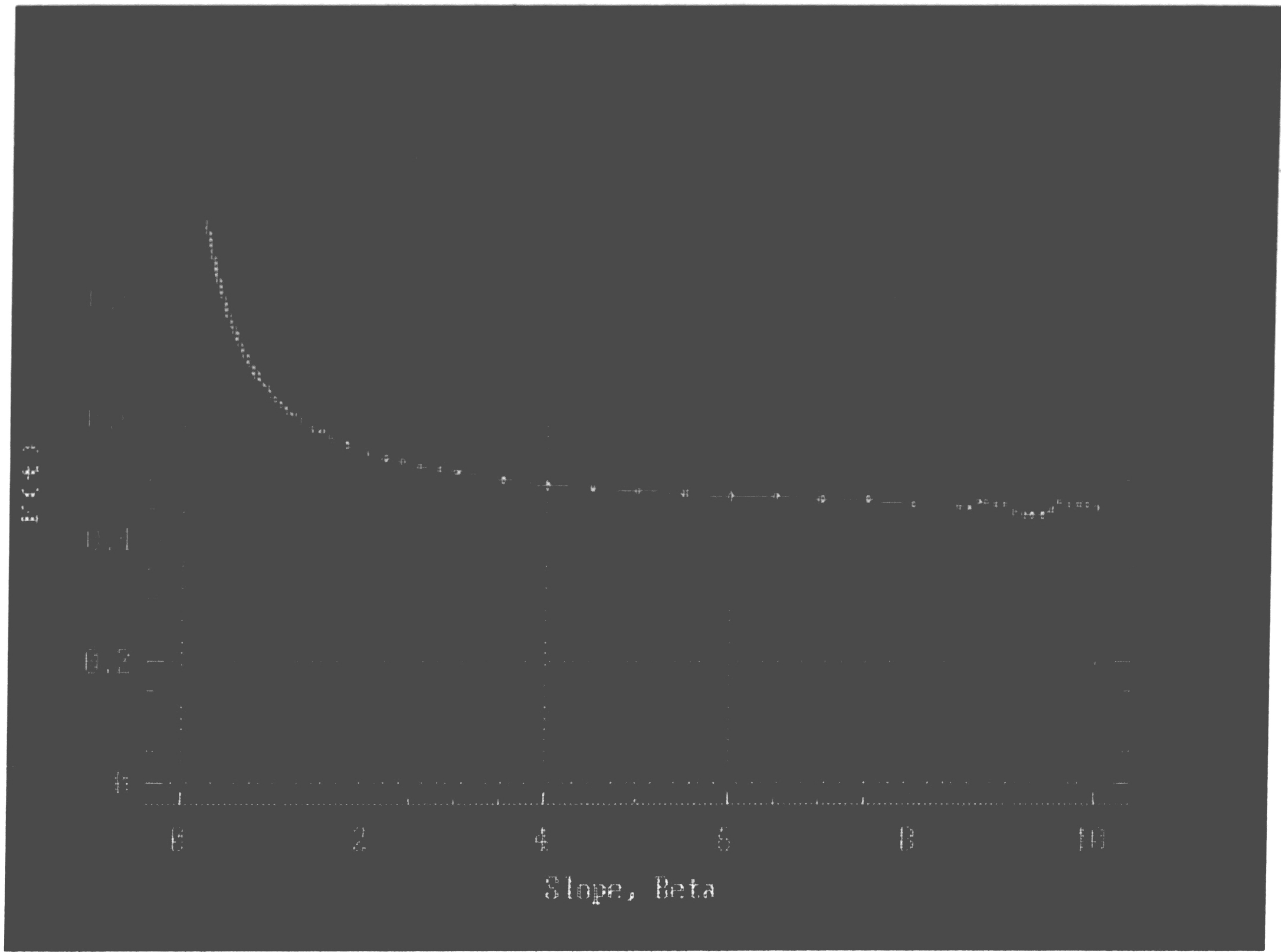

Figure 4. Cumulative Failure, F_{MTTF}, Plot

The FIT rate is the number of device failures which occur in 10^9 unit hours of operation and is calculated as follows:

$$\lambda = \frac{N_f \cdot 10^9}{Nt} \tag{17}$$

where N_f is the number of device failures after time t whether during service or on life/aging tests and N represents the total number of devices.

Random Failure Rate

The random failure rate can be calculated using an exponential distribution. If the devices are highly reliable, then the failure rate during service life should be small, almost zero; therefore one could assume that it is constant. Using the Weibull distribution for the reliability function R(t) using eq. (7) becomes

$$R(t) = \exp\left[-\frac{t}{\eta}\right] \tag{18}$$

with a slope, ß, of 1 (constant failure rate) and δ equal to zero.

Again for highly reliable devices the random failure rate may not be measurable. Therefore one must again use statistical methods to approximate the random failure rate. One approach as outlined in the work performed by British Telecom Research Laboratories [1], is to use a chi-squared distribution function as follows:

$$\lambda = \frac{\chi^2(N_f, C_L) * 10^9}{2NtA} \quad \text{FIT's} \tag{19}$$

where N_f is the number of failures at time t from the long-term aging test, C_L is the confidence level of the chi-squared distribution, N is the total number of devices on long-term aging, t is the length of the long-term age, and A is the long-term aging acceleration factor. See table 1 for chi-squared values at various confidence levels.

No. of Failures	Confidence Level			
	80%	90%	95%	99%
0	3.22	4.61	5.99	9.21
1	5.99	7.78	9.49	13.3
2	8.56	10.6	12.6	16.8
3	11.0	13.4	15.5	20.1
4	13.4	16.0	18.3	23.2
5	15.8	18.5	21.0	26.2

Table 1. Values of chi-squared [27]

To generate enough failures where the chi-squared statistics would not have to be used entails lengthening the long-term age. However, the length must be sufficiently short to avoid including device failures due to wear out.

As can be seen from EQ's (5) and (19) respectively, if the estimated activation energy is high then the acceleration factor A is high and the resulting FIT rate is optimistically low. It is important to use a conservative value of the activation energy if there is uncertainty in

its actual value. Otherwise the reliability calculations will be optimistically inaccurate.

Wear Out Failure Rate

Wear out failure rate can be calculated using two methods. The first method assumes a constant wear out failure rate and can be calculated by dividing the predicted number of wear out failures by the length of the service life. This value would then be added to the random failure rate to achieve a total failure rate. However, this assumes a highly reliable device with a constant failure rate.

To avoid any presumptions about the devices used in this study the method of calculating a maximum instantaneous failure rate will be used for calculating wear out failure rate during the service life.

The instantaneous failure rate is

$$\lambda(t) = \frac{10^9}{R(t)} \cdot \frac{dR(t)}{dt} \text{ FIT's} \tag{20}$$

applying the Weibull distribution for the reliability function $R(t)$, EQ

(7), the instantaneous failure rate becomes

$$\lambda(t) = \frac{\beta(t-\delta)^{\beta-1} * 10^9}{\eta^\beta} \quad \text{FIT's} \tag{21}$$

Taking the derivative of R(t) yields the maximum instantaneous or wear-out failure rate.

DEVICE FABRICATION

All InGaAsP pin photodetectors manufactured at AT&T have the same basic device structure. As can be seen in Figure 5 it is composed of a *n* doped InP substrate. The epitaxial layers are grown on top of the substrate using an Vapor Phase Epitaxial, VPE, growth technique composed of a slightly less *n* doped InP buffer layer and an intrinsic InGaAs active layer. The last three layers are the *n* doped InP cap layer, two silicon nitride layers one for diffusion masking the heavily *p* (Zn) doped junction and one to act as a anti-reflection/passivation layer with a Au ohmic contact centered over diffused region. The doping concentrations and layer thicknesses are in line with work published by AT&T Bell Laboratories engineers [26].

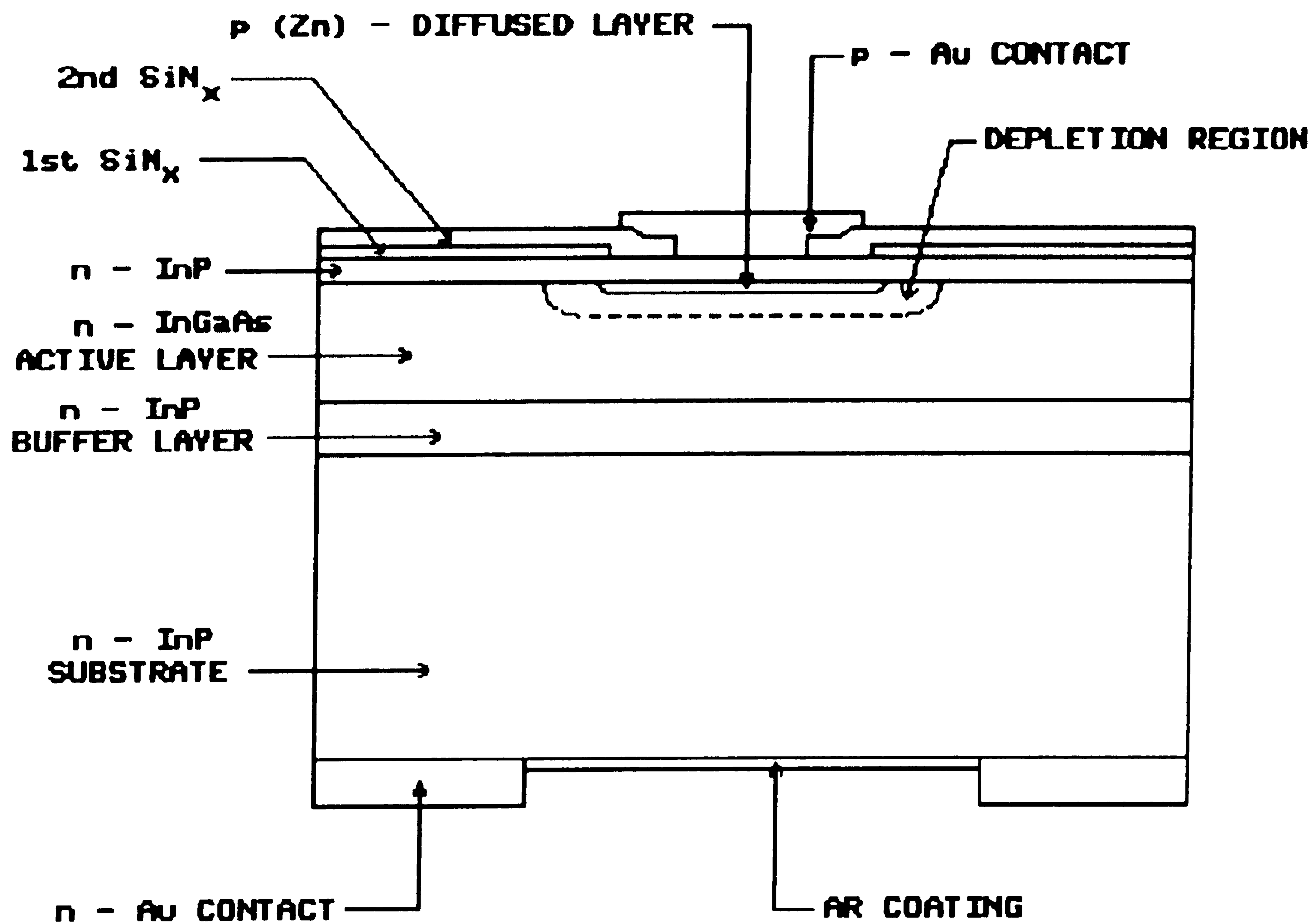

Figure 5. Structure of AT&T pin photodiode

A typical I-V curve can be seen in Figure 6. The two regions in the curve represent different physical phenomena which take place under the range of bias voltages shown. A detailed explanation of the phenomena as well as other parameters which are characteristic of this photodetector is available from material previously published by AT&T scientists [22],[26].

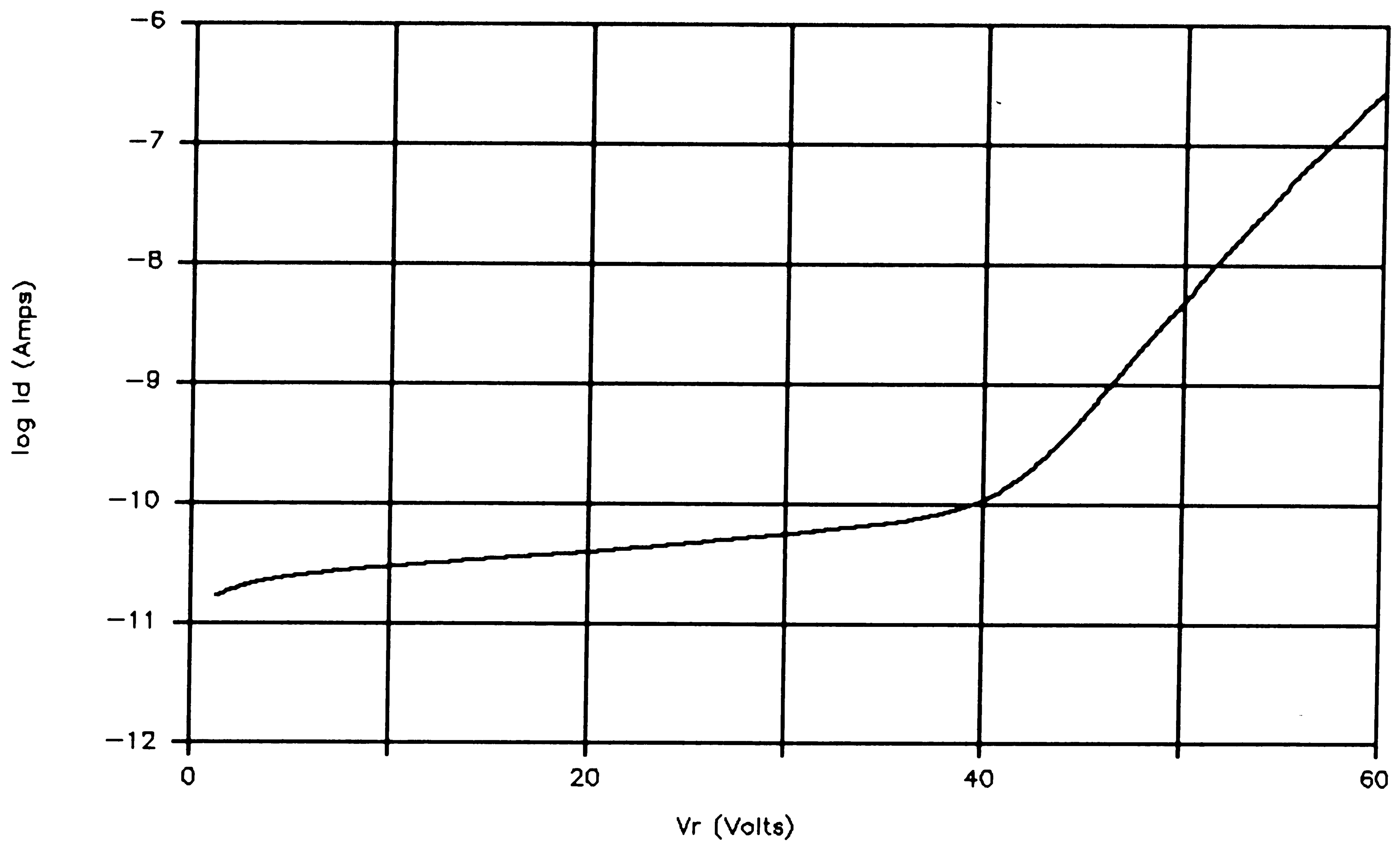

Figure 6. Typical I-V Curve for AT&T InGaAs pin Photodetector

The diffused junctions are fabricated with different diameters depending on each device application, and as can be seen in table 2 have different performance characteristics. Please note all electrical parameters are typical values measured at a reverse bias of 5 Volts.

Junc Diam (μm)	I_d (nA)	C_d (pF)	QE (%)	t_R (nS)	t_F (nS)	V_B (V)
76	<1	<.25	90	<.25	<1	>25
254	<10	<5	80	<2	<2	>25
381	<15	<9	80	<3	<3	>25

TABLE 2. AT&T long wavelength pin photodiode performance

The 76 μm junction photodetectors, primarily used in fiber optic receivers, are designed with a low capacitance for proper pre-amplifier design [21] as well as fast transition times. However, transition times are also dependent on the speed with which the undepleted carriers are swept out of the depletion region. This can be varied with the applied voltage which controls the intensity of the electric field in the depletion region. The 76 μm junction photodetectors are used in systems which operate up to 880 MBit/sec requiring bandwidths in excess of 1GHz i.e. risetimes less than 1 nS. The low dark currents are required for good S/N ratio which will be addressed in detail later. High quantum efficiency (QE), the efficiency of the photodetector converting photons to electrons, allows the downstream decision circuitry to distinguish between a logic 1 and logic 0 under low light level conditions. The breakdown voltage is an indication of the mechanical strength of the material when under electrical stress.

The 254 and 381 μm junction photodetectors are used primarily as optical monitors for the semiconductor laser based transmitters. They provide feedback to the laser current drivers in order to maintain a constant optical power output. The capacitance is not a speed issue since the photodetector supplies a DC feedback current. Since the photodetector is sufficiently close to the laser the lower quantum efficiency of the photodiode, i.e. lower detection current, is offset by a larger active region. Again because the photodetector is being used as a feedback mechanism the larger dark current, due to the larger junction, is not an issue in terms of a S/N ratio.

Long Term Aging Monitors

An increase in dark current, I_d, is the dominate failure mode for pin photodetectors. The two major causes of an increase in dark current during the service life are electrostatic discharge (ESD) or other transients and random or wear-out failures.

ESD or transient induced damage is usually characterized by a sudden increase in dark current, even shorting of the diode. The ESD or transient causes a large amount of current to pass quickly through a very small region of the junction inducing high current densities. The damage is physically characterized by a localized "blow-out" or melting of material usually located on the periphery of the *p-n* junction. The use of electron beam induced current, EBIC, imaging highlights the

material damage in the form of a bright spot. The EBIC technique will be discussed in detail in a future section. This study had one diode which failed during the aging and is attributed to ESD/transient exposure.

Random or wear-out failures, the focus of this study, exhibit a gradual increase in dark current during aging. The dark current values at which a device can be considered a failure varies. Various studies [7],[14],[16],[20] categorize a device failure as being the point at which the dark current exceeds 100 nA for a pin photodetector with a typical dark current of 10 nA. Others suggest a dark current reading which is ten times the initial value [4],[5],[9-12]. For this study, the dark current limit will be set at 100 nA. The impact of photodetector dark current increase on system performance will be evaluated in a future section.

The breakdown voltage in the reverse direction is another indicator of device performance degradation [3],[7],[14],[20]. The failure mode is a low breakdown voltage and is characterized by the tunneling "knee" either being located near the operating voltage or shifting to the left during device operation. The "knee" of the I-V curve in Figure 5 occurs at a reverse bias voltage of 40 Volts. This parameter was monitored throughout the aging study and confirms the results of earlier work as mentioned above.

A test method developed at AT&T Bell Laboratories by J. V. Gates II at Murray Hill, NJ is used to characterize the dark current stability of

AT&T manufactured long wavelength pin photodetectors. The test method involves plotting two passes of the I-V curves of a photodiode from 0 to 60 Volts, see Figure 7. Typically the features of interest are the leakage current at the operating bias (5 Volts), the amount of hysteresis between the first and second I-V trace, and the steepness of the slope of the leakage current. The leakage current is a function of the diffusion, generation-recombination, and tunneling of electrons [22]. The fabrication process determines to what extent each of the three contributes to the leakage current. Hysteresis could be attributed to charge trapping centers in the bulk of the semiconductor near the depletion region. The hysteresis affect would be a resultant of the charge centers filling and releasing majority carriers which cross the depletion region. A large amount of work was performed during the development of these photodiodes such that these features are virtually nonexistent but are continually monitored as an indication of process quality.

The measurement of interest is the dln(I)/dV {dI/dV}. Using the I-V data, the derivative of the natural logarithm of the current is divided by the derivative of the applied voltage and is also plotted from 0 to 60 Volts as can be seen in Figure 7. Because prodabations in the dark current tend to be small and are undetectable with a standard current meter, the first order derivative is used to detect the prodabation in current with increasing applied voltage. The two important features of interest in the dI/dV are the location of the tunneling "peak" which occurs at the "knee" of the I-

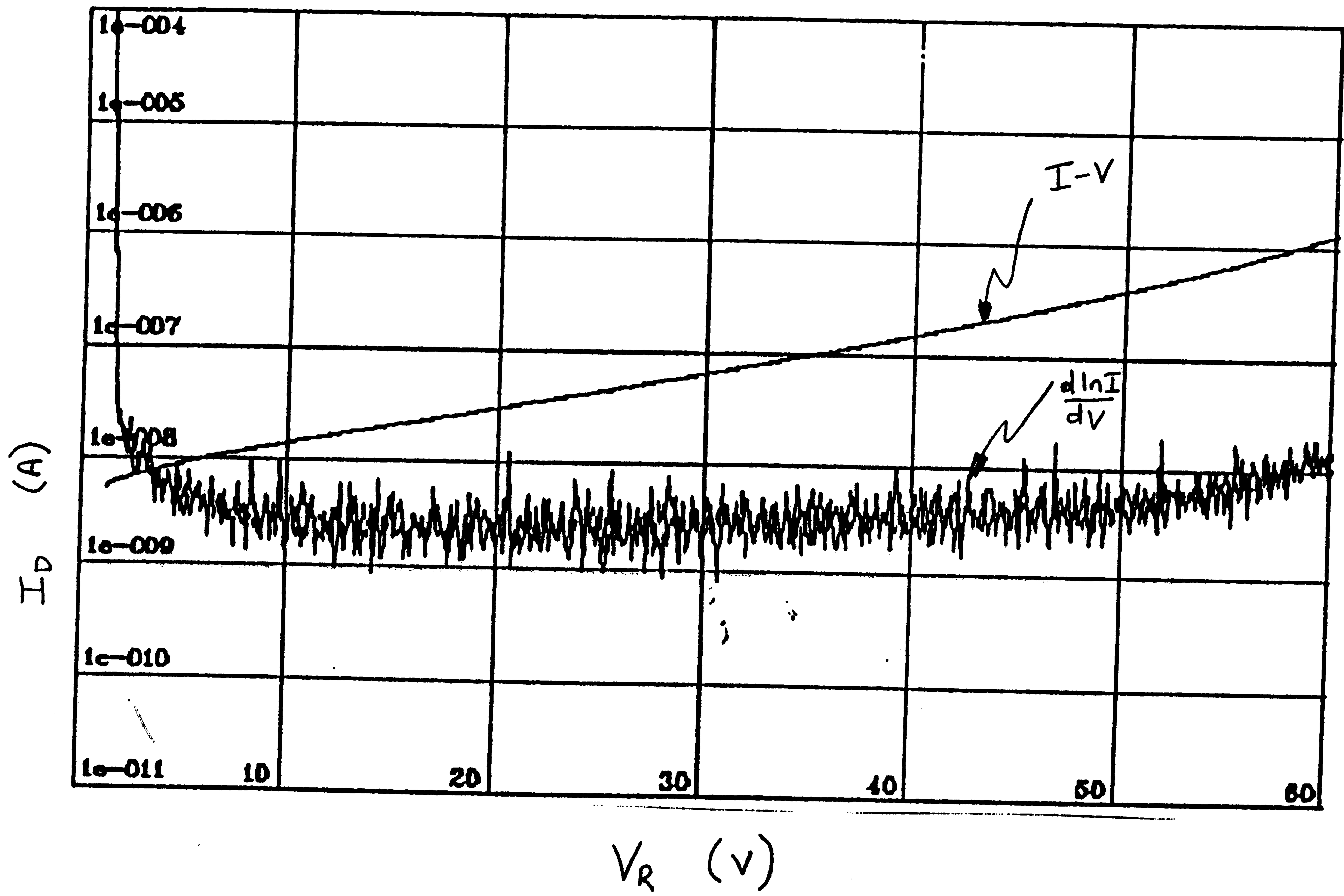

Figure 7. Typical I-V, dI/dV Trace

V curve and the noise which occurs as a result of the change in current as the applied voltage increases.

Again the tunneling "peak" or "knee" is the breakdown voltage, an indication of the mechanical strength of the material to an applied voltage. The location of the breakdown voltage is a stable feature and is also monitored as an indication of process quality. The "noise" in the dI/dV curve is assigned a numerical value which is related to the cumulative amplitude over a voltage window of typically 5 volts. This noise value is used to categorize devices based on the value of the noise at each voltage "window" and on the cumulative noise for each trace over the entire sixty volt range. For the purposes of this study photodiodes were placed into three categories based on the cumulative noise "rating" of the dI/dV measurement: low noise (total noise amplitude ranging from 0 to less than 3) see figure 8, mid-noise (total noise amplitude ranging from greater than 3 to less than 7) see figure 9 and high noise (total noise amplitude greater than 7) see figure 10.

Some unpublished work has been done by AT&T Bell Laboratories to understand the relationship between dI/dV noise and the long term reliability of InGaAs pin photodetectors grown with liquid phase epitaxy (LPE) and other device structures such as ternary and quaternary structures. This study will be the first comprehensive work performed on the VPE grown binary InGaAs pin photodetectors currently made by AT&T.

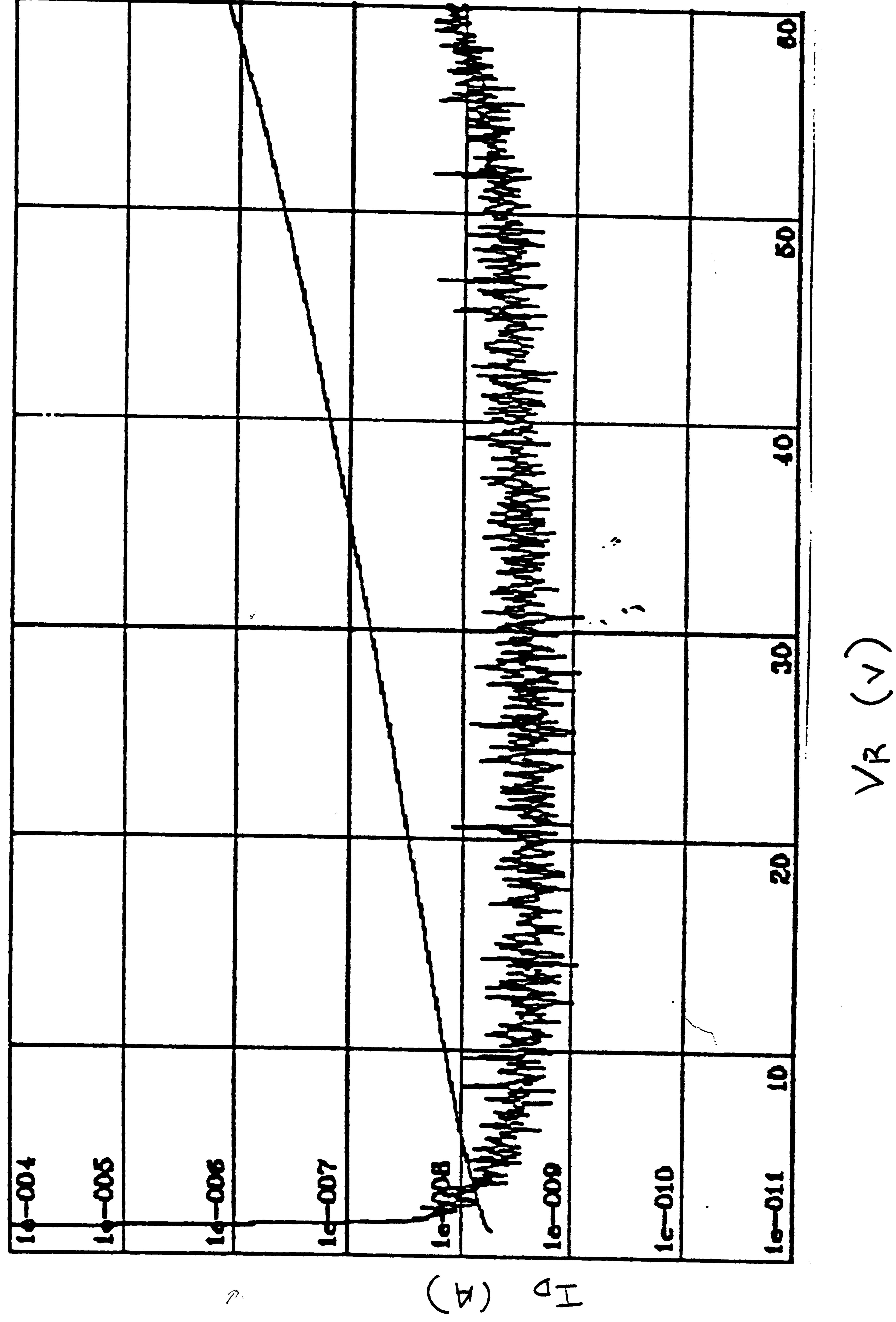

FIGURE 8. TYPICAL LOW NOISE dI/dV TRACE

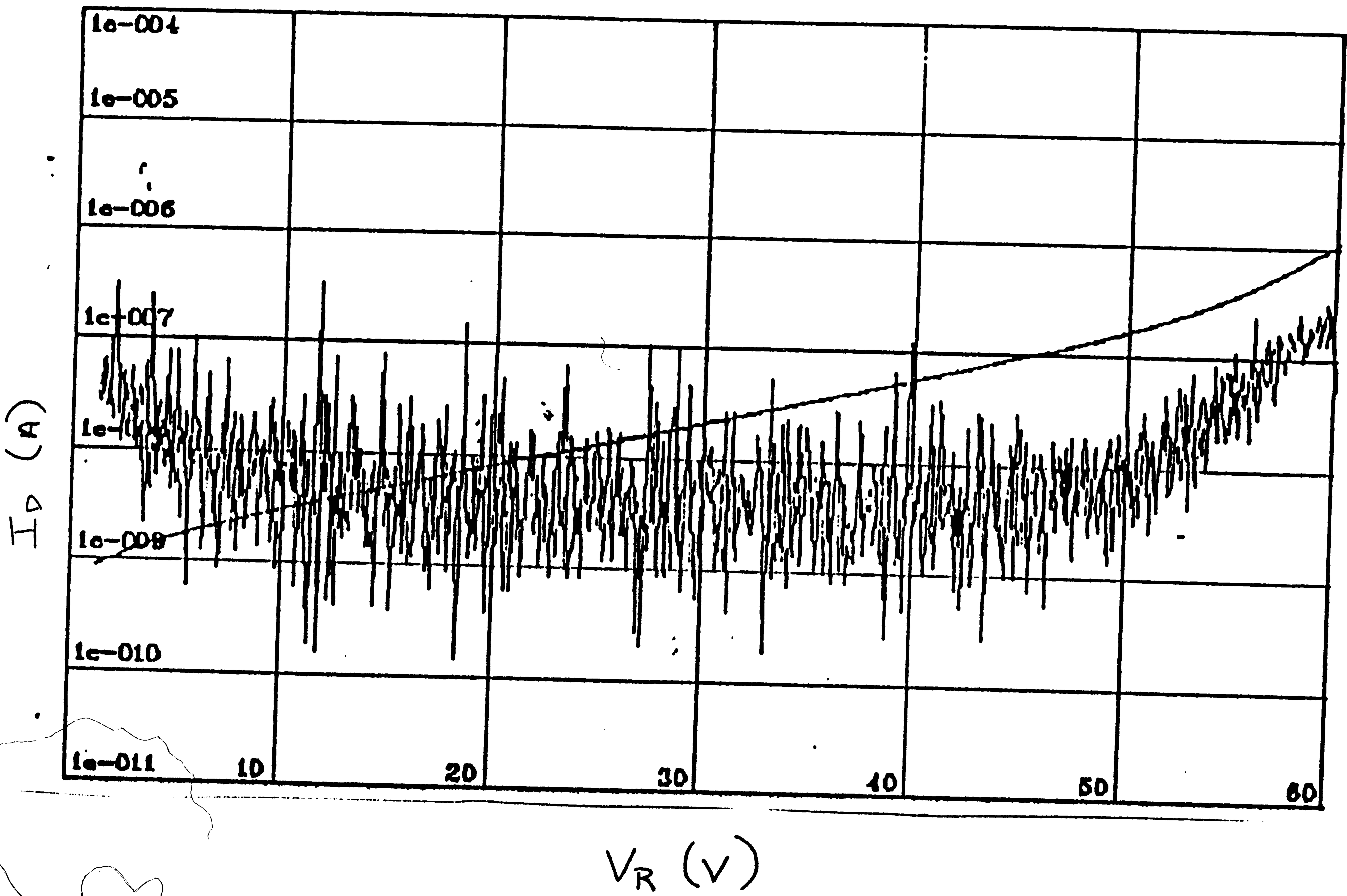

FIGURE 9. TYPICAL MID NOISE dI/dV TRACE

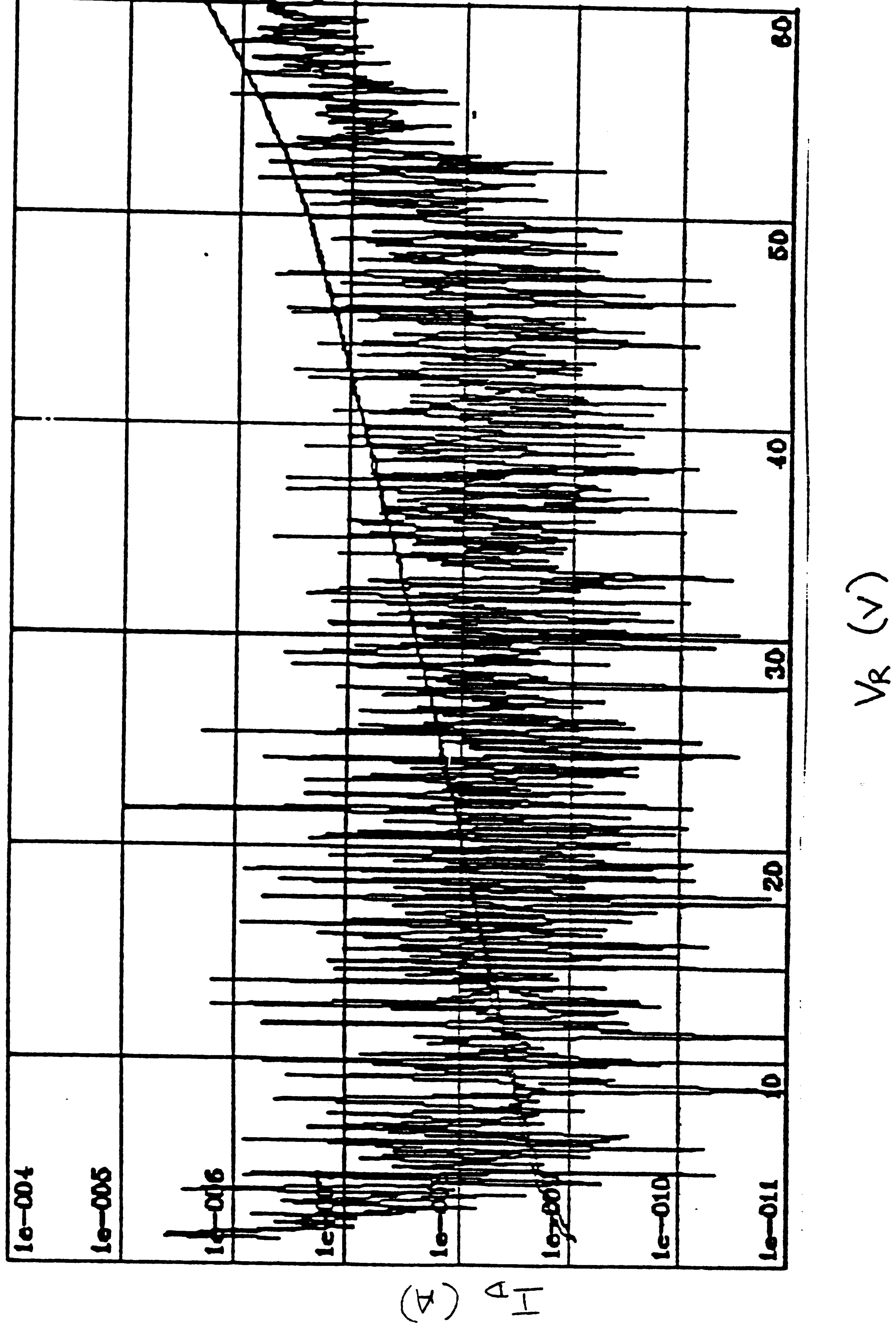

FIGURE 10. TYPICAL HIGH NOISE dI/dV TRACE

The intention is to see if there is an identifiable "signature" in the dI/dV which can be attributed to failure modes that occur during the weed-out of infant failures during device burn-in and ultimately long term aging. If so, this would provide manufacturing with a tool to possibly eliminate BI for the screening of infant failures and random failures from the population of devices going into the field to reduce the actual long term failure rate. The correlation to BI and long term aging will be discussed in detail in a future section.

The source of noise in the dI/dV trace is unknown. Many theories exist on the origin of dI/dV noise; however, it is beyond the scope of this study to find the cause. A good understanding of device physics is required to begin to understand the noise phenomena. Some of the theories currently held follow. If the noise source is surface related, it could be due to pin holes in the silicon nitride located above or within a minority carrier diffusion length of the junction area. If the pin hole is longer than a diffusion length away from the depletion region, any leakage current or trapped charge will recombine before entering the depletion region. These pin holes are possibly a result of debris left on the surface of the semiconductor before deposition of the nitride material. Pin holes could create a leakage path for current. Another surface related affect is the non-uniform creation of the junction edges due to mask defects. The non-uniformities would allow for non-uniform electric fields which could cause localized breakdown. Both pin holes and junction definition defects allow for the presence of

extra leakage current and the possible creation of microplasmas [5],[12],[14],[15],[20],[23-25].

If the noise sources are bulk related, it could be a defect center located within a diffusion length of the depletion region in the bulk of the semiconductor. This defect center would either trap and release or generate charge, causing prodabations of the leakage current. If the defect is located near the depletion region, it could be captured as the depletion region expands as a result of the applied voltage. These bulk defects could be caused by improper device fabrication as each layer is grown or propagate from some defect which is present in the epitaxial substrate material surface. Work is ongoing to study both surface and bulk phenomena.

Ideal photodiodes would show little or no dark current. Stable increases in dark current as a function of increased bias should show little noise if the material is defect free since the junction will grow and the dark current will scale with area having a predictable diffusion, tunneling, gen-rec characteristics [22] i.e no prodabations. One purpose of this study is to determine if the noise source(s), highlighted by a noisy dI/dV trace, negatively impact the length of device life. To take it one step further can dI/dV predict HTHB, infant mortality, failures. If so, it could mean significant reduction in testing and burn-in of production devices.

Other previously published work indicates that other parameters such as capacitance, rise/fall times and quantum efficiency have not changed before catastrophic changes occurred in the dark current [3],[7],[15],[16]. This study monitored these parameters throughout the aging study and confirm the results of other authors.

SYSTEM REQUIREMENTS

Most of the published literature to date claim FIT rates for photodetectors with similar materials and device structures of less than 1 FIT. Systems which use the photodetectors require FIT rates which are typically less than 1 FIT. These studies were primarily for undersea application where the use of the fiber optic cable and its associated repeater stages exceed 25 year lifetimes before reaching obsolescence [8],[21]. Obviously, terrestrial requirements are less stringent where it is less expensive for field repair and obsolescence is reached at an earlier time, 3 to 10 years depending on the application.

Device failures which occur instantaneously, the device is effectively shorted, are easier to pinpoint in a system than a device which experiences a gradual degradation. The shorted device can be located via probing different nodes in the fiber optic link or if the capability exists by having the system preform a regressive check of a link from one end point to another.

The device which degrades gradually over time is difficult to "find" in the system. This is due to its subtle effect on system performance in the form of signal-to-noise S/N ratio degradation. A lower S/N ratio causes errors in the information or bit-stream that is being sent through the fiber either at the regenerating, repeater, stage or at the receiver stage above and beyond the number of errors which the system is capable of recovering. The S/N for a typical optical fiber receiver is calculated as follows:

$$\frac{S}{N} = \frac{\langle i_p^2 \rangle}{2q(I_p + I_D)B + 2qI_LB + 4kTB/R_L} \qquad (22)$$

where

q - charge of an electron, 1.6x10-19 C

I_p - photocurrent of photodetector

I_D - bulk dark current

B - bandwidth of the system

I_L - surface leakage current

k - Boltzmann's Constant, 8.63×10^{-5} eV/^{o}K

T - absolute temperature in ^{o}K

R_L - load resistance

and $<i_p^2>$ is the sinusoidally varying input signal component and is of the form

$$<i_p^2> = \frac{m^2}{2} I_p^2 \qquad (23)$$

where *m* is a modulation index related to LED's and laser's as a ratio of the variation of bias current delta I and the bias current I_B.

If typical values of

I_p - 6 μA @ 50 μW incident light

$I_D + I_L$ - .5 nA

B - 880 mB/s

T - 300 ^oK

R_L - 10^4 Ohm

m - .85

are used for a pin photodetector and respective fiber optic receiver, using EQ (22) the *S/N* ratio is 36.16 dB. If the photodetector bulk dark current and surface leakage current combined start to degrade over time to 100 nA, 500 nA, 1 μA, 2 μA the *S/N* ratio will also degrade as 36.12 dB, 35.97 dB, 35.78 dB, 35.44 dB respectively. The penalty for photodetector degradation in the receiver performance can be as much as .7 dB as can be seen from the above calculations. The effect on system

performance in terms of introducing errors into the information stream depends on the dynamic range of the receiver and the optical power margin between transmitter and receiver. The .7 dB drop in *S/N* ratio with respect to the dynamic range, typically 20 dB, is insignificant. However, if the power budget is on the order of 2-6 dB the .7 dB reduction can affect the system performance.

The photodetectors in this study showed a rapid increase in dark current over time once the value of dark current exceeded 100 nA. Therefore the failure criteria for devices used in this study was any device whose absolute dark current value exceeded 100 nA during aging.

EXPERIMENT OUTLINE

The pin photodetectors used in this study were selected at random from the manufacturing line. The intention was not to bias the selection process by choosing "hero" devices, but selecting typical product which experienced normal day-to-day processing variation.

The photodetectors were selected from 28 different wafers providing a good cross-section of production material. A total of 147 photodiodes were aged at 200 Degrees Celsius and 146 at 250 Degrees Celsius. Tables 3 & 4 below outline the matrices of junction size versus dI/dV noise rating for the photodetectors used in this study.

Junc Size (μm)	dI/dV Noise Rating			
	Low	Mid	High	I-V Ratio
76	14	15	19	NA
254	14	15	16	NA
381	15	-	34	15

TABLE 3. 200 Degree Celsius Matrix

Junc Size (μm)	dI/dV Noise Rating			
	Low	Mid	High	I-V Ratio
76	18	15	21	NA
254	16	14	1	NA
381	18	-	36	7

TABLE 4. 250 Degree Celsius Matrix

The I-V ratio category corresponds to photodiodes with an abnormally steep I-V slope in the tunneling region. The I-V ratio characteristic is predominantly found in the photodiodes with a 381 μm junction diameter. Since the noise is low, the intention is to concentrate on the I-V ratio "signature" and determine if it has any significant impact on the long term reliability of the photodetector.

In addition, the mid and high noise category for the 381 μm junction devices were combined. There was not a clear distinction between the mid and high noise categories as in the other two junction size devices. Again the intent is to analyze the relationship, if any, between noise in the dI/dV traces and device reliability.

Equipment Set-Up

The test equipment and ovens used for this experiment are detailed in Diagram 1. The life test was a monitored age, leakage current was measured through-out aging at 200 and 250 degrees Celsius in separate chambers. For each chamber an AT&T 6300 PC, age computer, was used as the controller for all hardware. A Hewlett-Packard 6209B power supply was used for biasing the devices during aging. A Keithly 706 scanner was used to scan through all devices and make a leakage current measurement about every 20 milliseconds. A Keithly 196 Digital Multi-Meter was used to take the measurements. The multimeter was actually measuring the voltage drop across a current divider consisting of a 100 KOhm resistor and another resistor with a value which was determined by two factors. First, the Keithly multi-meter was used in the .1 to 3V range, its highest accuracy, where its internal impedance is > 1 GOhm, effectively infinity. Therefore, the voltage drop across the divider should not exceed 3V within ±100%. Second the leakage of the photodiodes at 200° C varies from .1 μA to 30 μA and 250° C from 1 μA to 300 μA. Therefore, the resistance value of the other resistors were 50 KOhm and 9 KOhm for

200 & 250 degree Celsius operation respectively to allow the leakage currents to increase as the devices age without affecting the measurements. Delta Design 9064 chambers were used to bring the devices to temperature and hold to a ±.5 °C accuracy. The chambers used liquid nitrogen to return the devices to room temperature for periodic dark current measurements.

An additional AT&T PC 6300, "crunch" computer, is networked with each age computer with an IEEE-488 card. It's sole responsibility is to gather data during and after each aging run and to plot the age data.

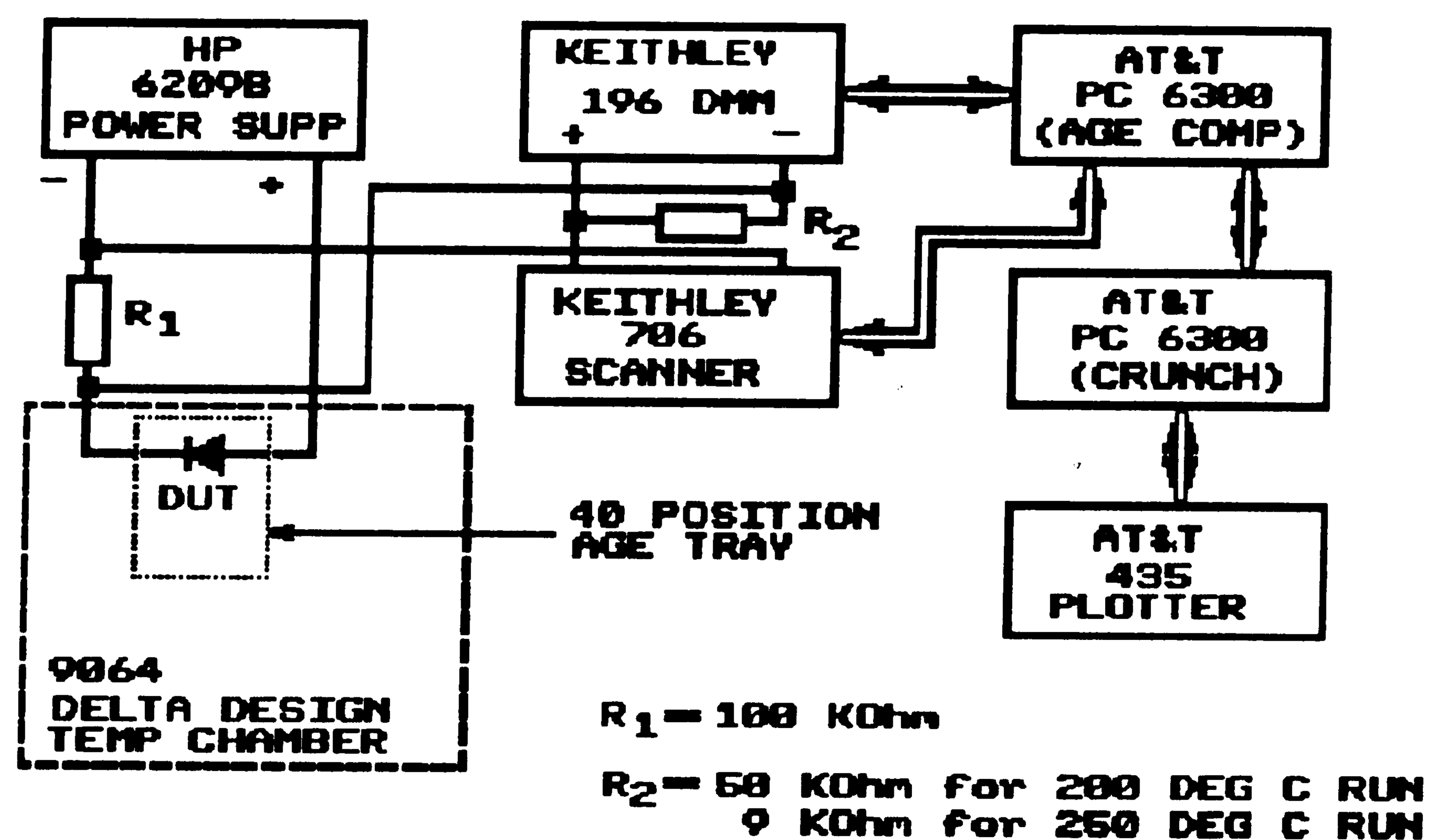

Diagram 1. Long Term Aging System Configuration

All software is written in C source code and compiled using a DeSmett-C88 compiler. The software integrates the functions of: creating files

for data collection during aging; bringing the ovens to temperature, hold the ovens at temperature for approximately 40 minutes to allow junction temperature to reach chamber temperature; turn on device bias; set-up DMM for proper ranging; operate scanner to monitor leakage current for each device during aging, and create a summary file of date of run, device serial number, min & max leakage current, and the delta of the two.

High temperature aging boards were used which accept a high speed ceramic package in which all photodiodes were eutectically bonded using a AuGe solder. A 95% lead, 5% Tin alloy solder with a melting point of 270-312°C was used on all hardware solder joints to withstand the extreme temperatures within each chamber.

All equipment connections, with the exception of computer to computer interface which used RS-232 connections, used GP-IB interfaces.

Collected Data

All devices were measured for dI/dV, V_B was determined from the dI/dV plot, and I_d at time zero, time prior to the start of aging. The dI/dV measurement was made prior to HTHB to see if there was any correlation to burn-in failures. Dark current was measured approximately weekly and dI/dV was checked on devices as the dark currents started to shift to check for changes in the noise of the trace as well as shifts in the

breakdown voltage. A sample of 3 photodiodes from each dI/dV noise group were also measured for quantum efficiency, risetime/falltime, and capacitance. Both dI/dV and other parametric data are time consuming measurements so they were measured at t=2470 hours for the 200 Degree Celsius group and t=2307 hours for the 250 Degree Celsius group.

RESULTS

The dark current data for all devices used in the study compared to the dI/dV cumulative noise suggested a interaction between the two. A regression analysis was performed on the dI/dV cumulative noise vs dark current for each group of diodes with the same junction size. The groups were analyzed separately due to the differences in the average value of the dark current for each group which is directly related to the junction size. The correlation for each group is as follows: 76 μm diameter, R = -.19; 254 μm diameter, R = -.44; and 381 μm diameter, R = -.37. These correlation values suggest a very weak dependence of the cumulative noise on the value of the dark current.

The correlation of dI/dV cumulative noise rating to burn-in results had a coefficient of R = -.22. Table 5 below shows the quantities of devices which failed burn-in, i.e. dark current shifts greater than 5 nA and in the case of 381 μm diameter junction devices greater than 2 nA.

Junc Size (μm)	Wafer	Noise Rating	Burn-In Failure Mode delta I_d (nA)
76	165171-302	4.24 (mid)	27.4
254	165515-9	8.32 (high)	SHORT
	165515-35	8.87 (high)	29.6
	165815-60	2.11 (low)	SHORT
	165795-396	21.35 (high)	31.5
	166485-402	7.14 (mid)	-5.4
	166485-407	4.96 (mid)	-6.5
	165735-412	3.04 (mid)	6.6
	165735-415	4.44 (mid)	-7.1
	165785-474	20.55 (high)	8.3
	165495-505	5.29 (mid)	SHORT
381	16536-257	4.87 (mid)	2.8
	16536-258	3.70 (mid)	3.1
	16536-260	6.05 (mid)	5.3
	16555-526	14.31 (high)	-4.8

Table 5. Burn-In Failures

The burn-in failures listed above are weakly correlated to the value of the cumulative noise in the dI/dV trace. In addition, there is not a dependence on the wafer identity. The lack of correlation suggests that the dI/dV trace does not have a noise feature which lends itself to predicting the success of passing burn-in. Upon comparing the dI/dV traces for other devices which passed burn-in there were no visible features which distinguished the failures from the rest of the population.

As mentioned earlier the breakdown voltage in these devices behaved similarly to results published in other papers. That is, prior to the dark current degrading in an aging failure the breakdown voltage shifted below the value measured at t=0.

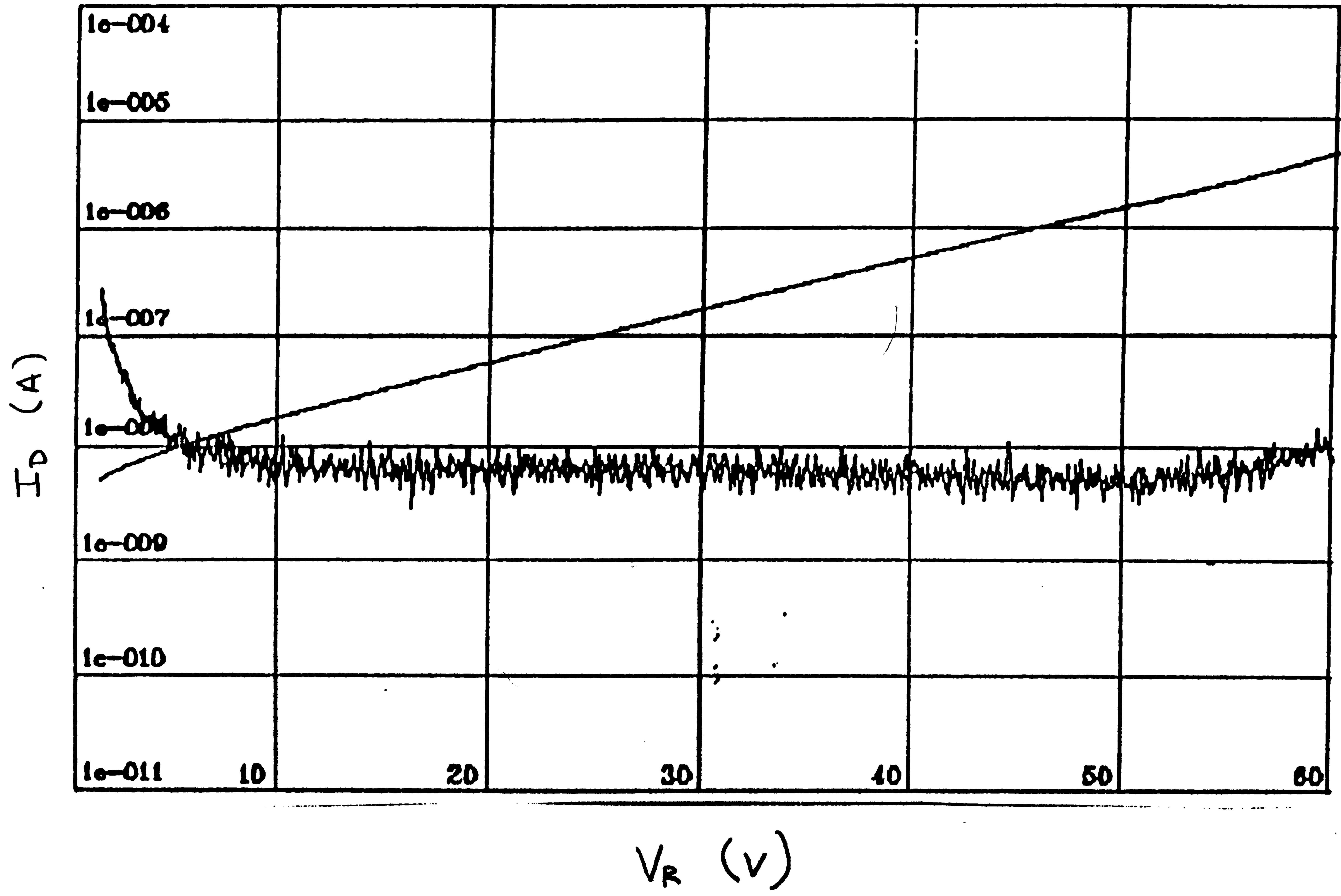

FIGURE 11. DEVICE # 56 @ t = 0 HOURS

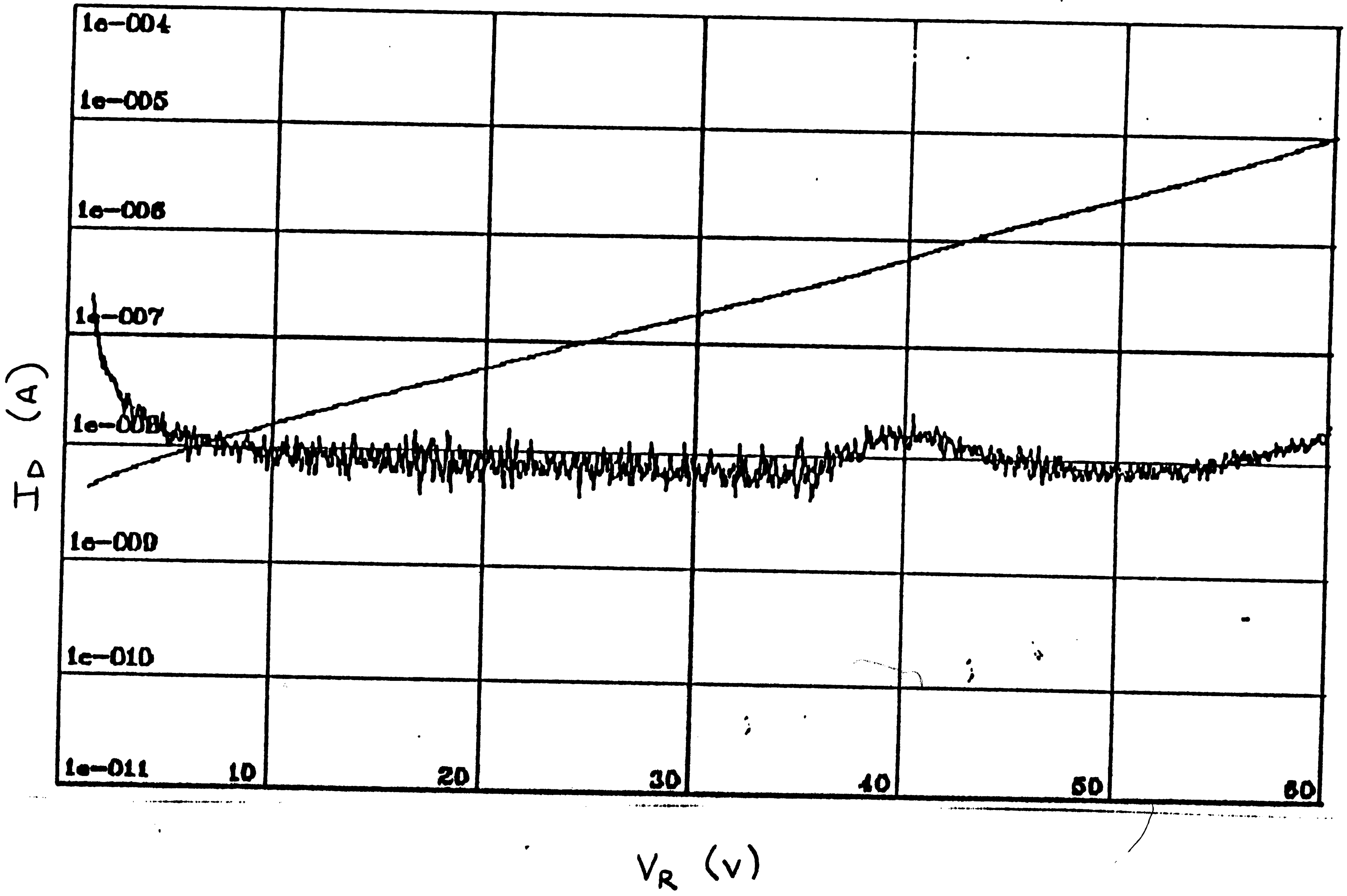

FIGURE 12. DEVICE #56 @ t=1326 HOURS

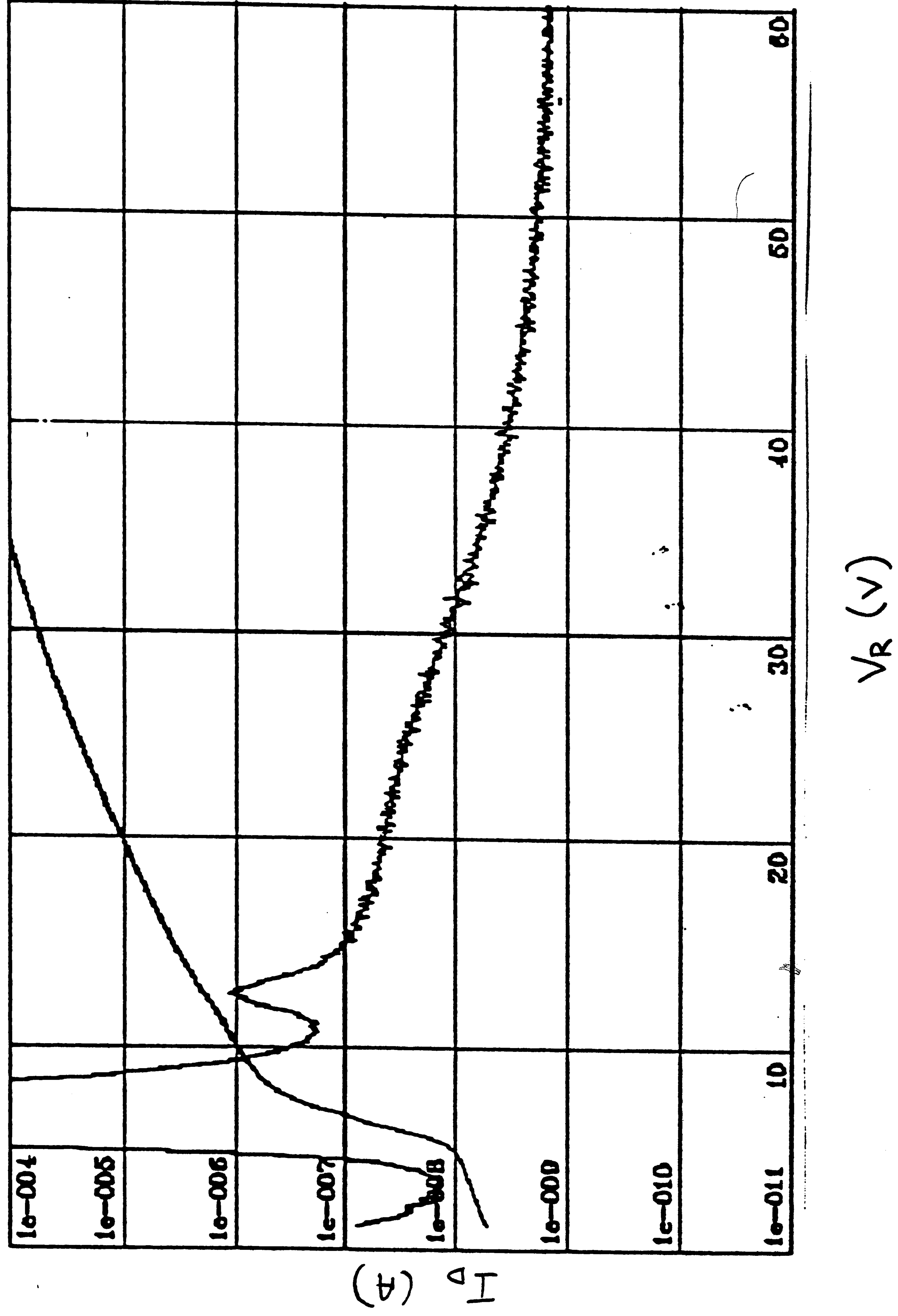

FIGURE 13. DEVICE #56 @ t= 2307 HOURS

As can be seen in Figure 11 (device 56) the breakdown voltage started at some value greater than 60 Volts, the actual value is outside the measuring range for the dI/dV test. At t=1326 hours another dI/dV reading as taken, see Figure 12, a "hump" starts to appear in the dI/dV trace at about 40 Volts showing the breakdown voltage moving in and is visible in the "knee" on the I-V trace. Further aging perpetuates this phenomena and at t=2307 hours a final dI/dV trace was taken, see Figure 13, and as expected the breakdown voltage has shifted almost to the operating voltage of 5 Volts. At this point device 56 has a dark current at 5 Volts of 9.5 nA which is an increase of 2 nA from its initial reading. Dark current readings taken after t=2307 hours show continual degradation.

As mentioned earlier dI/dV measurements were taken at t=2470 hours for the 200 Degree Celsius group and t=2307 hours for the 250 Degree Celsius group. The 200 Degree Celsius group has not shown any failures after 4303 hours. Comparing the dI/dV traces for both t=0 and t=2470 there is no apparent change in the shape or amount of noise present in both the I-V or the dI/dV curve. Figures 14-16 displays the dark current readings for the 200 Degree Celsius group taken for each junction size and noise category used in the study. The dark current readings are extremely stable for all groups of devices regardless of junction size and cumulative dI/dV noise.

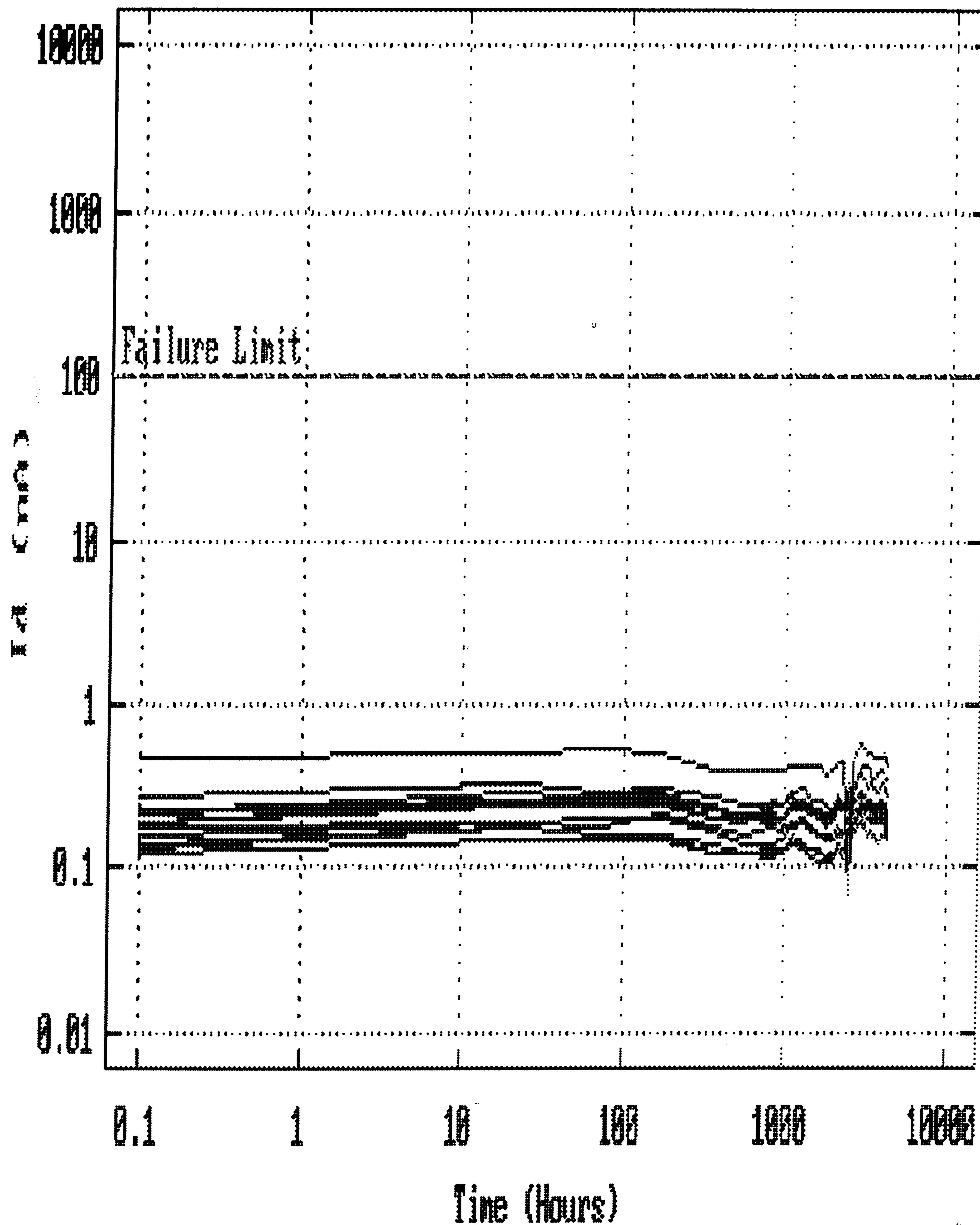

Figure 14(a) Dark Current for 76 μm Diameter Junction Device @ 200 Degree Celsius, High dI/dV Noise

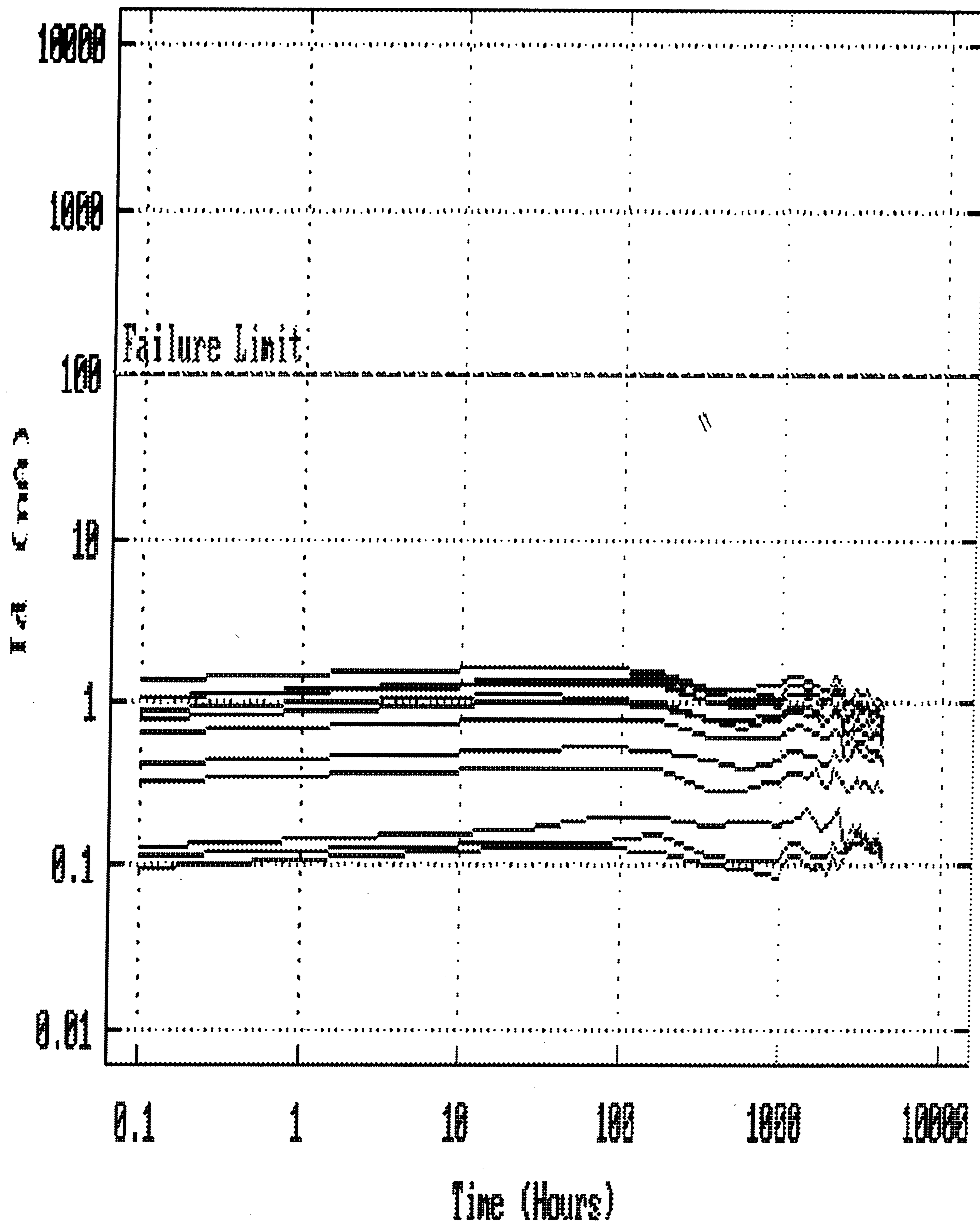

Figure 14(b) Dark Current for 76 μm Diameter Junction Device @ 200 Degree Celsius, Mid dI/dV Noise

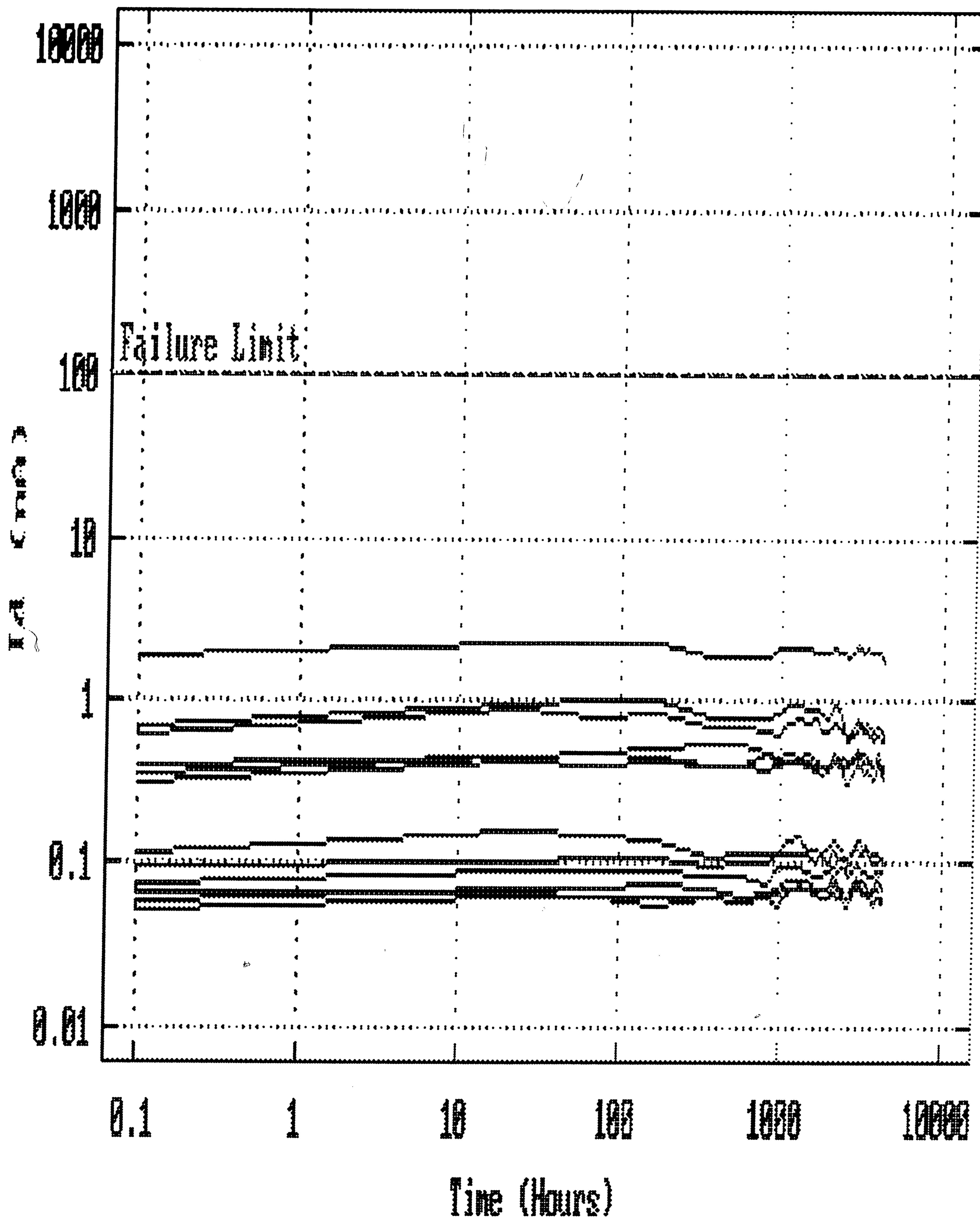

Figure 14(c) Dark Current for 76 μm Diameter Junction Device @ 200 Degree Celsius, Low dI/dV Noise

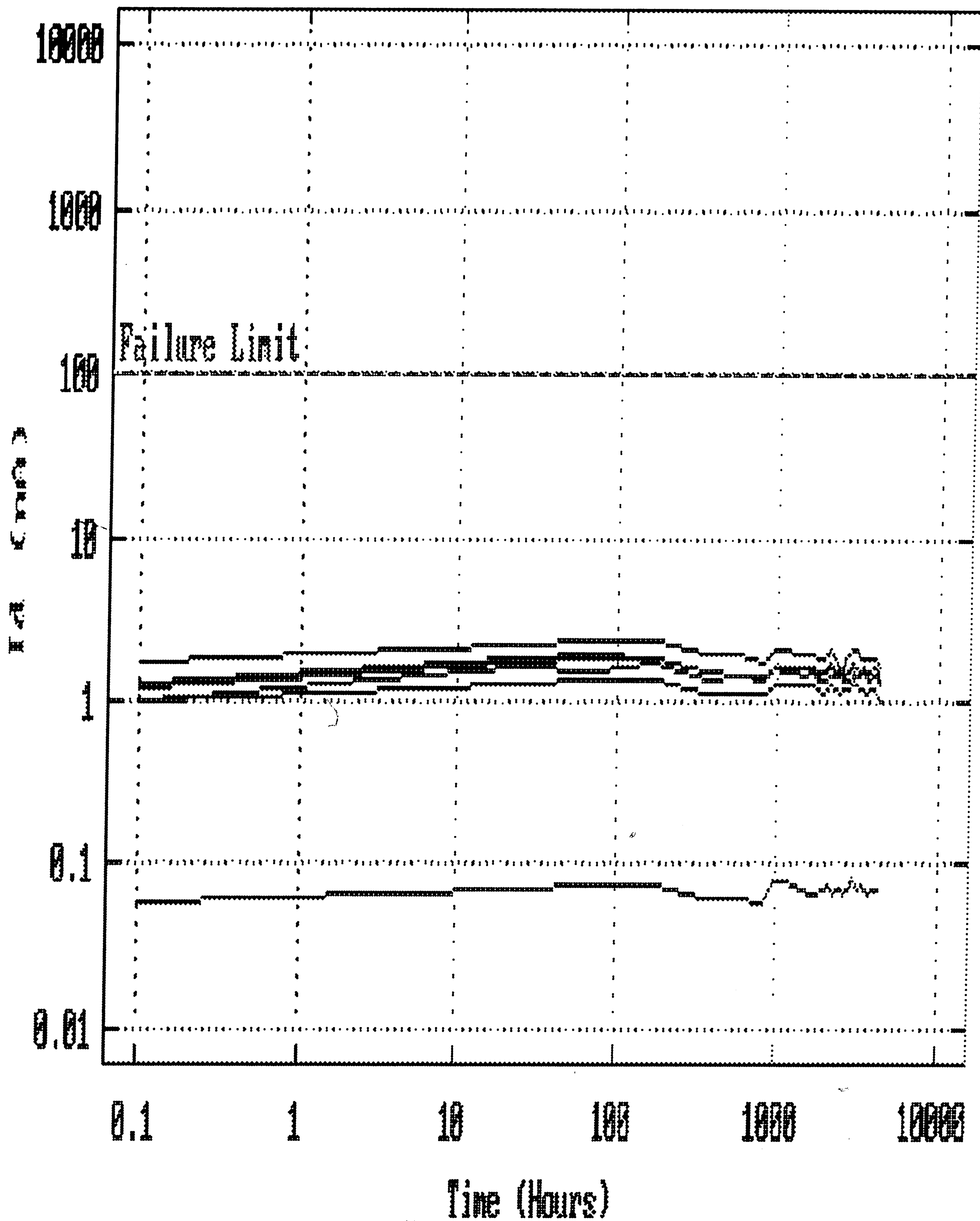

Figure 15(a) Dark Current for 254 μm Diameter Junction Device @ 200 Degree Celsius, High dI/dV Noise

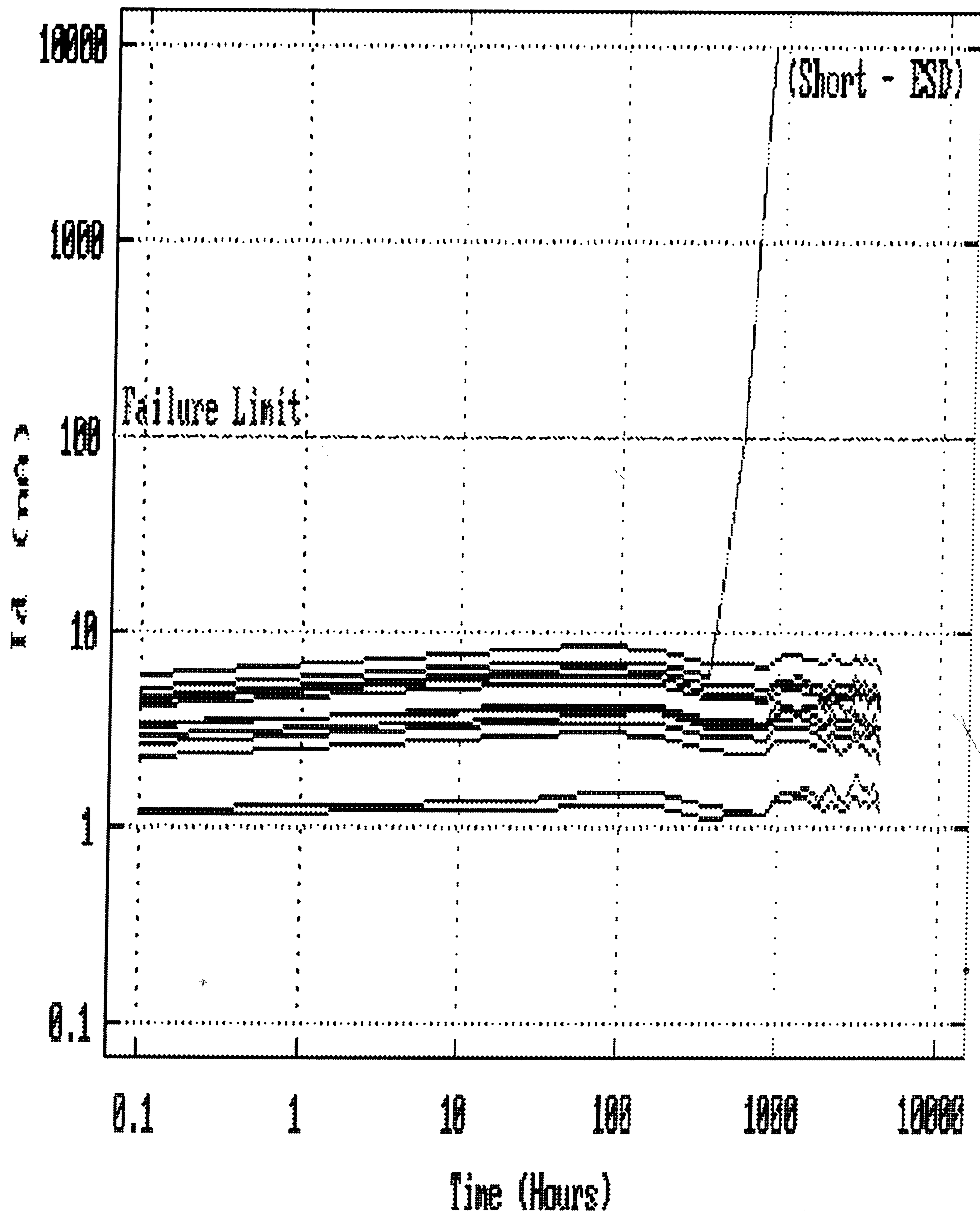

Figure 15(b) Dark Current for 254 μm Diameter Junction Device @ 200 Degree Celsius, Mid dI/dV Noise

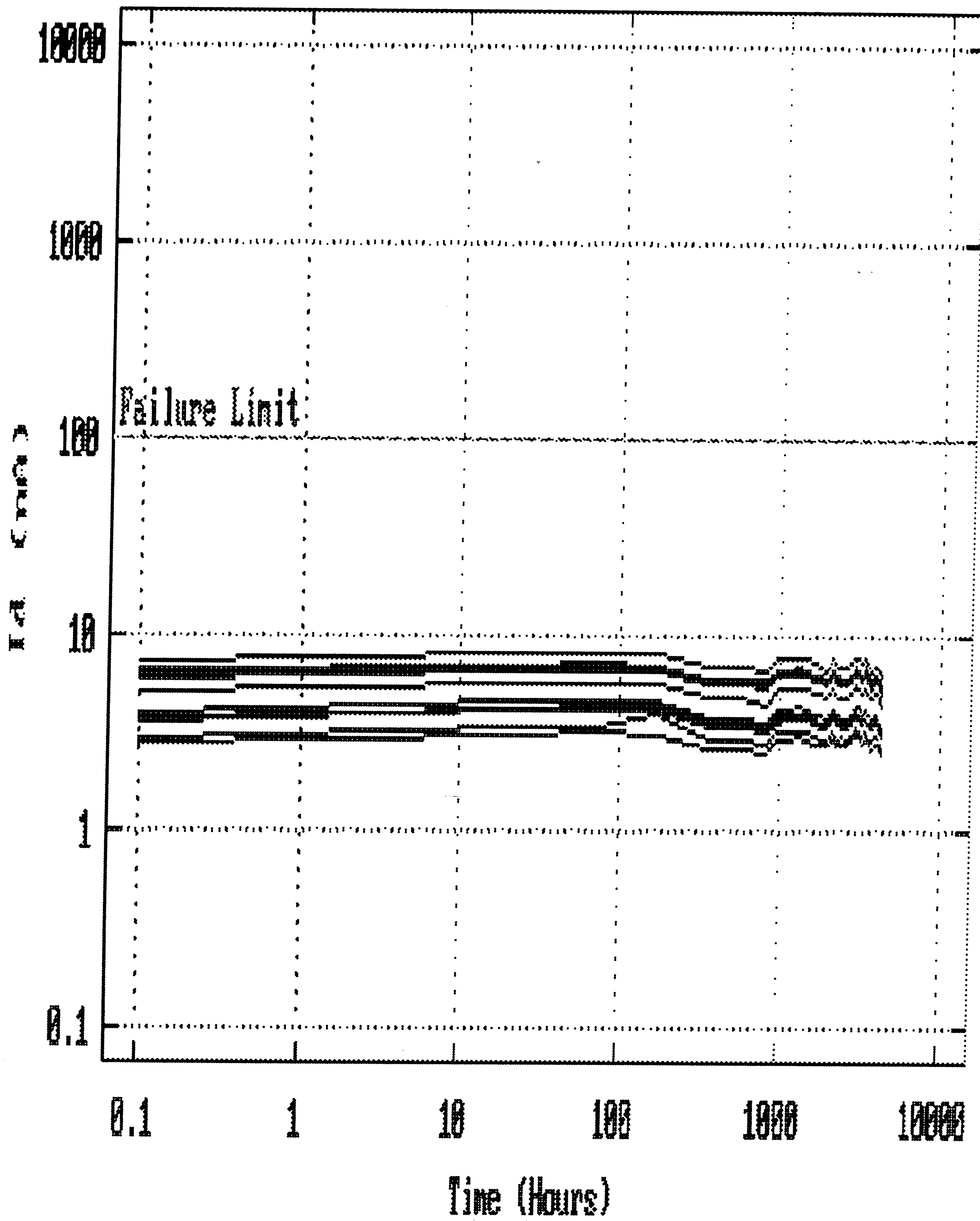

Figure 15(c) Dark Current for 254 μm Diameter Junction Device @ 200 Degree Celsius, Low dI/dV Noise

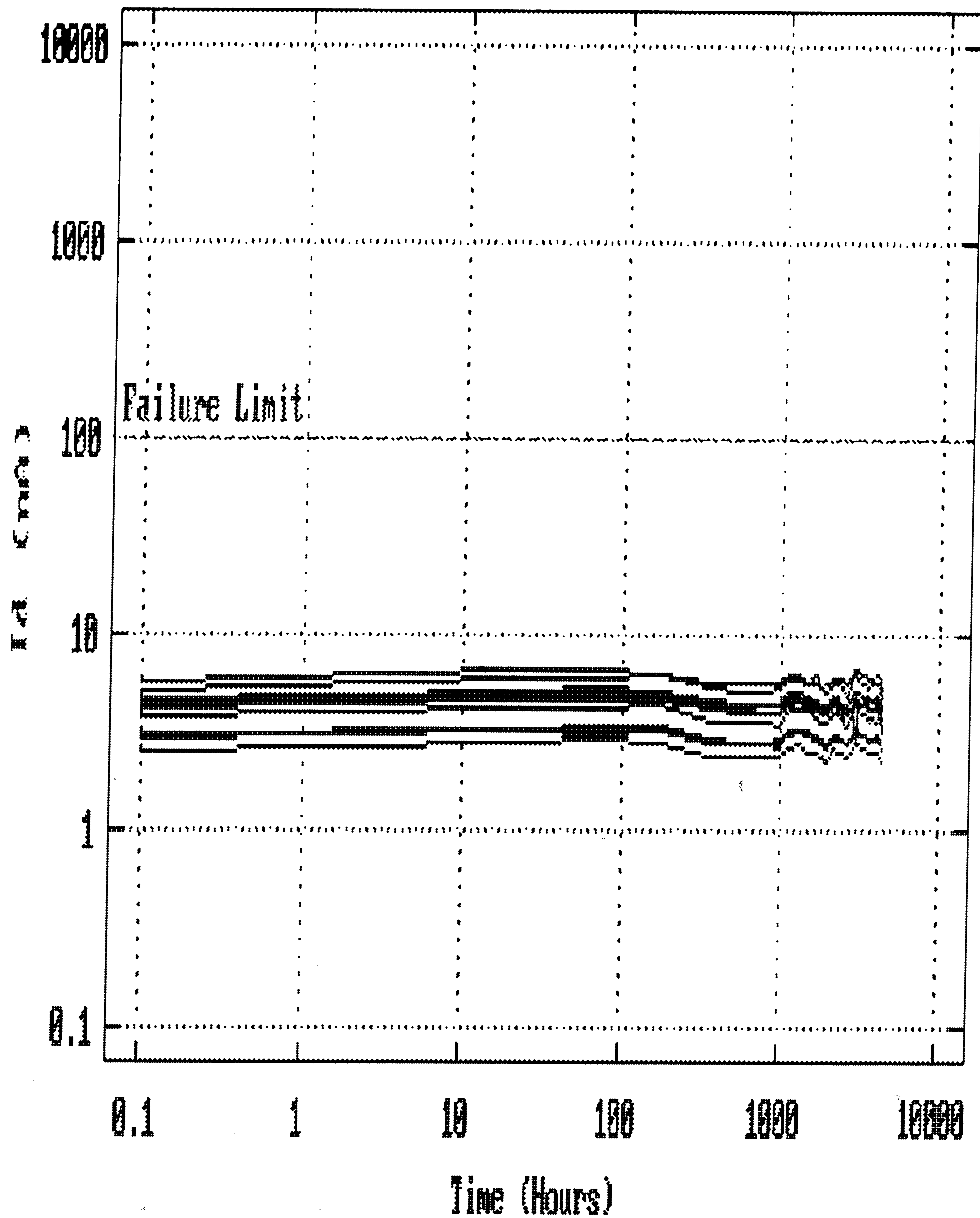

Figure 16(a) Dark Current for 381 μm Diameter Junction Device @ 200 Degree Celsius, High dI/dV Noise

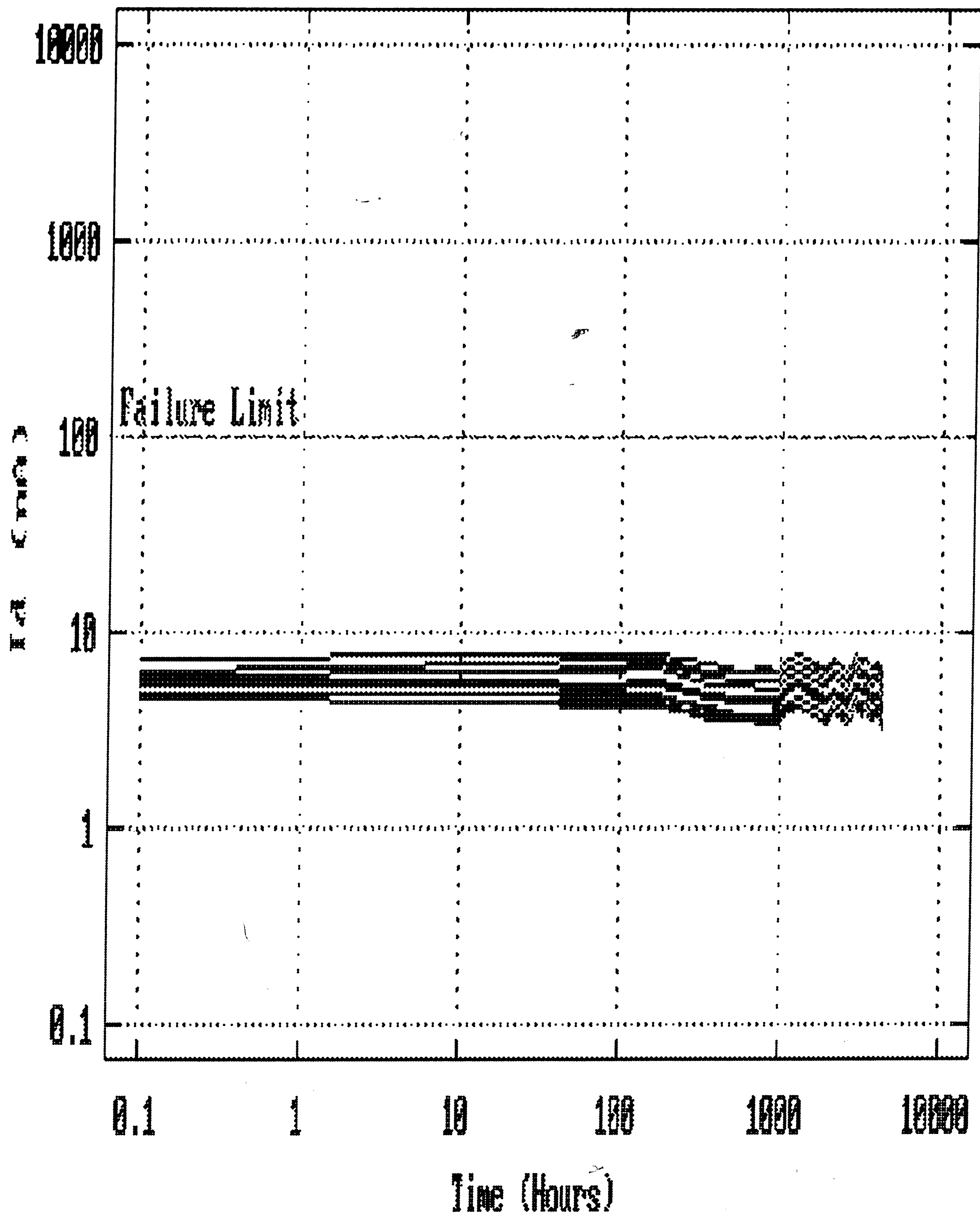

Figure 16(b) Dark Current for 381 μm Diameter Junction Device @ 200 Degree Celsius, High I-V Ratio, Low dI/dV Noise

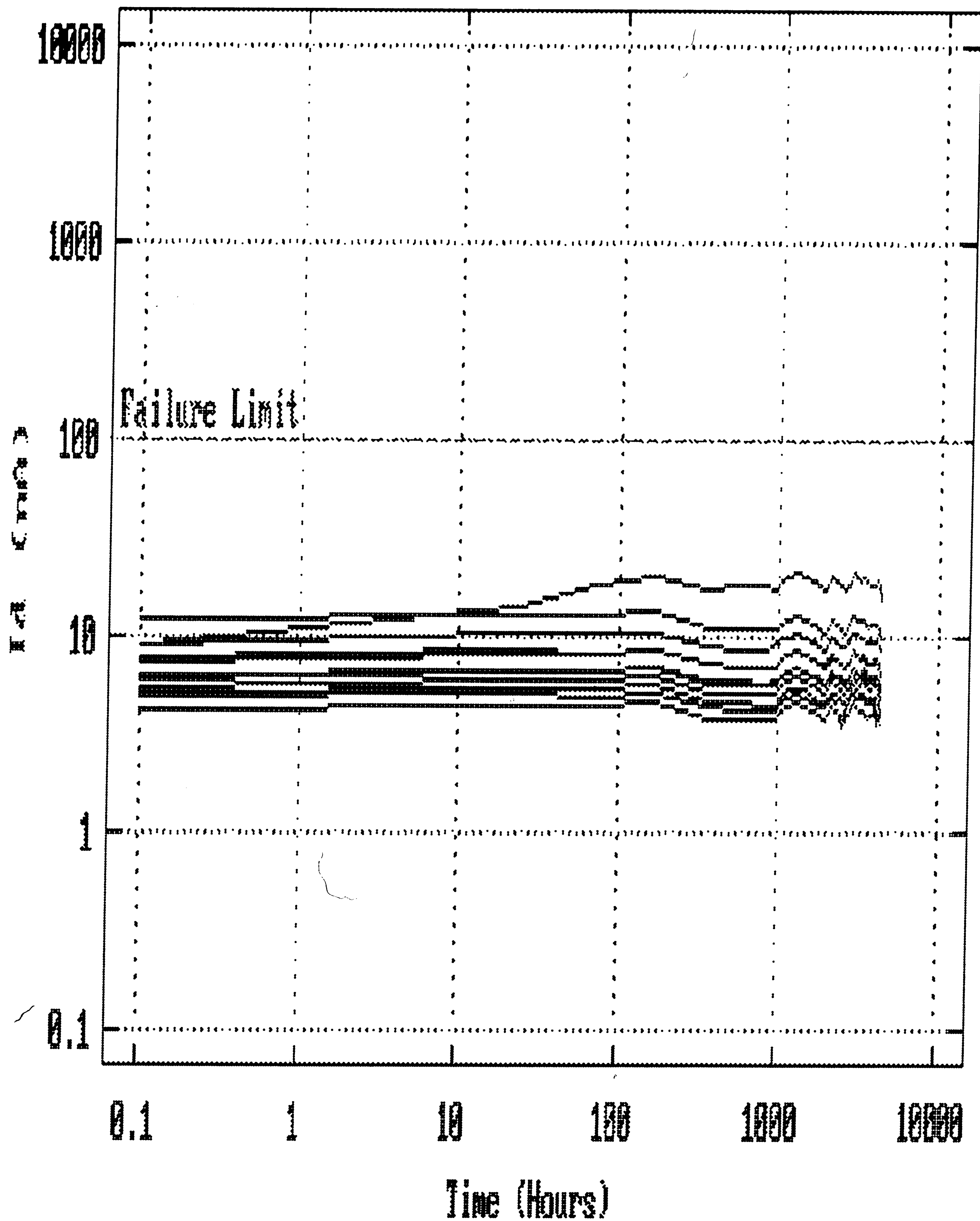

Figure 16(c) Dark Current for 381 μm Diameter Junction Device @ 200 Degree Celsius, Low dI/dV Noise

Junc Size (μm)	Wafer	Noise Rating	Time I_D Fail Occurred t=(hours)
76			
254			
381	165550-510	2.86 (low)	1987
	165550-515	4.87 (mid)	2393
	165550-518	4.38 (mid)	1821
	165550-524	8.9 (high)	2393
	165550-528	2.81 (low)	1987
	165550-541	6.22 (mid)	1987

Table 6. 250 Degree Celsius Aging Failures

The 250 Degree Celsius group started to show aging failures as displayed in Table 6. Once again there was not a feature in the dI/dV trace when measured at $t=0$ which distinguished devices with drifting dark currents during aging from the rest of the population of "good" devices. Figure 17-19 displays the dark current readings for the 250 Degree Celsius group taken for each junction size and noise category used in the study. The dark current readings are stable for all groups of devices with the exception of the high noise 381 μm diameter junction devices. At $t=2590$ this group showed a total of six failures as displayed in Table 6. Since there were no failures in the 200 Degree Celsius population, the 250 Degree Celsius devices which started to shift and ultimately fail aging will be evaluated to determine if in fact these devices are wear out failures. The larger area photodiodes would be expected to fail first due to either random or wear-out failure since a larger quantity of thermally activated defects would be located within the active region of the device.

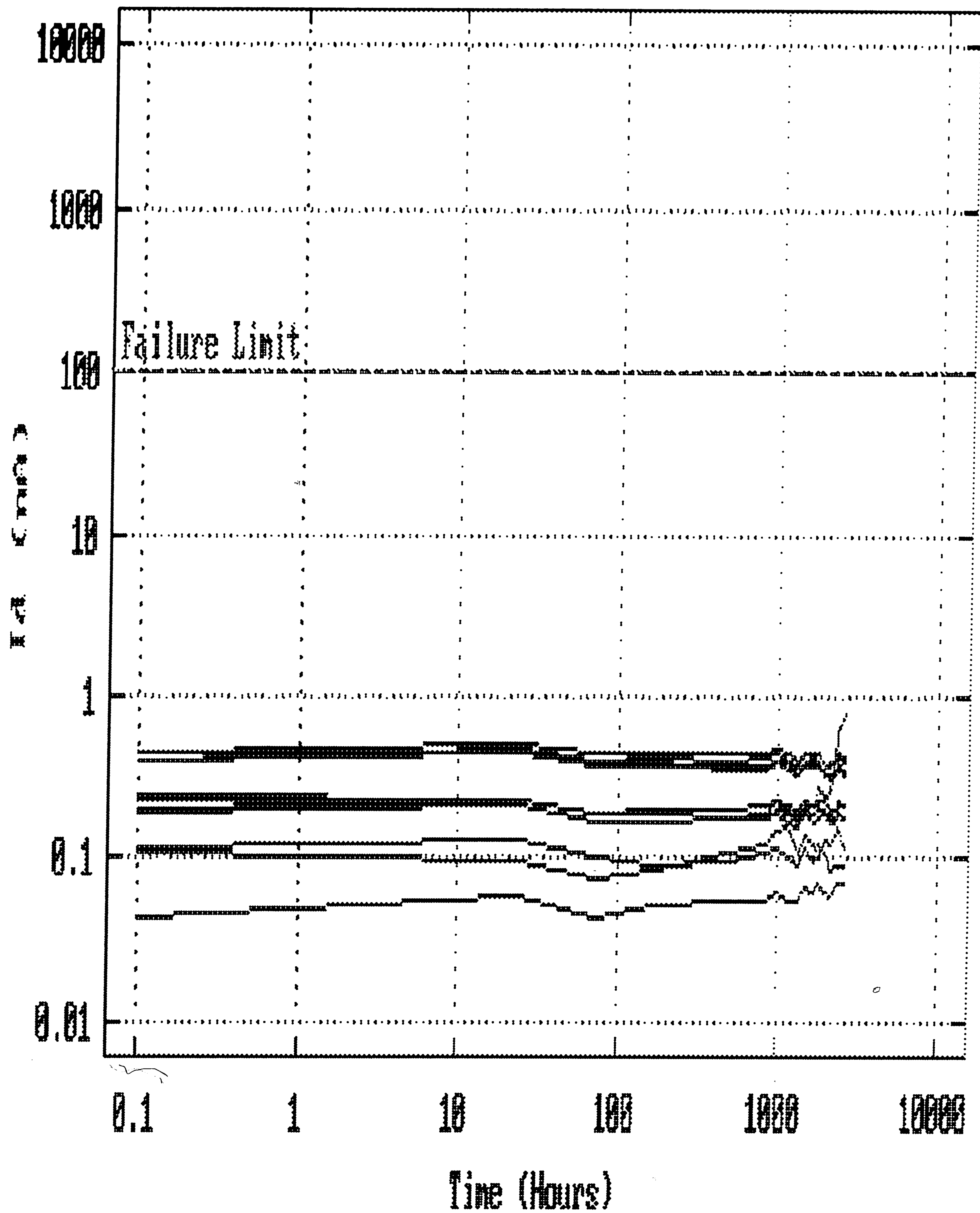

Figure 17(a) Dark Current for 76 μm Diameter Junction Device @ 250 Degree Celsius, High dI/dV Noise

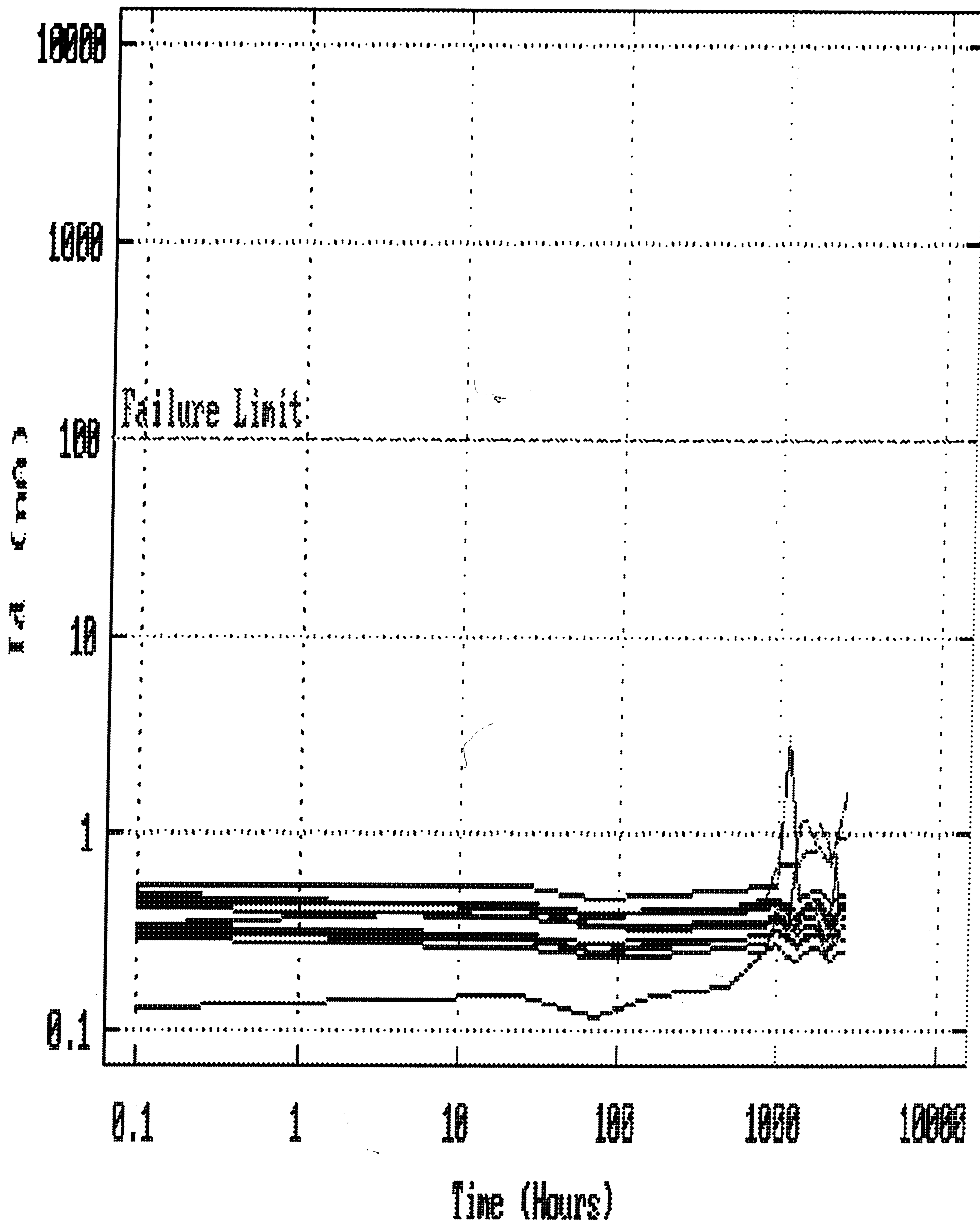

Figure 17(b) Dark Current for 76 μm Diameter Junction Device @ 250 Degree Celsius, Mid dI/dV Noise

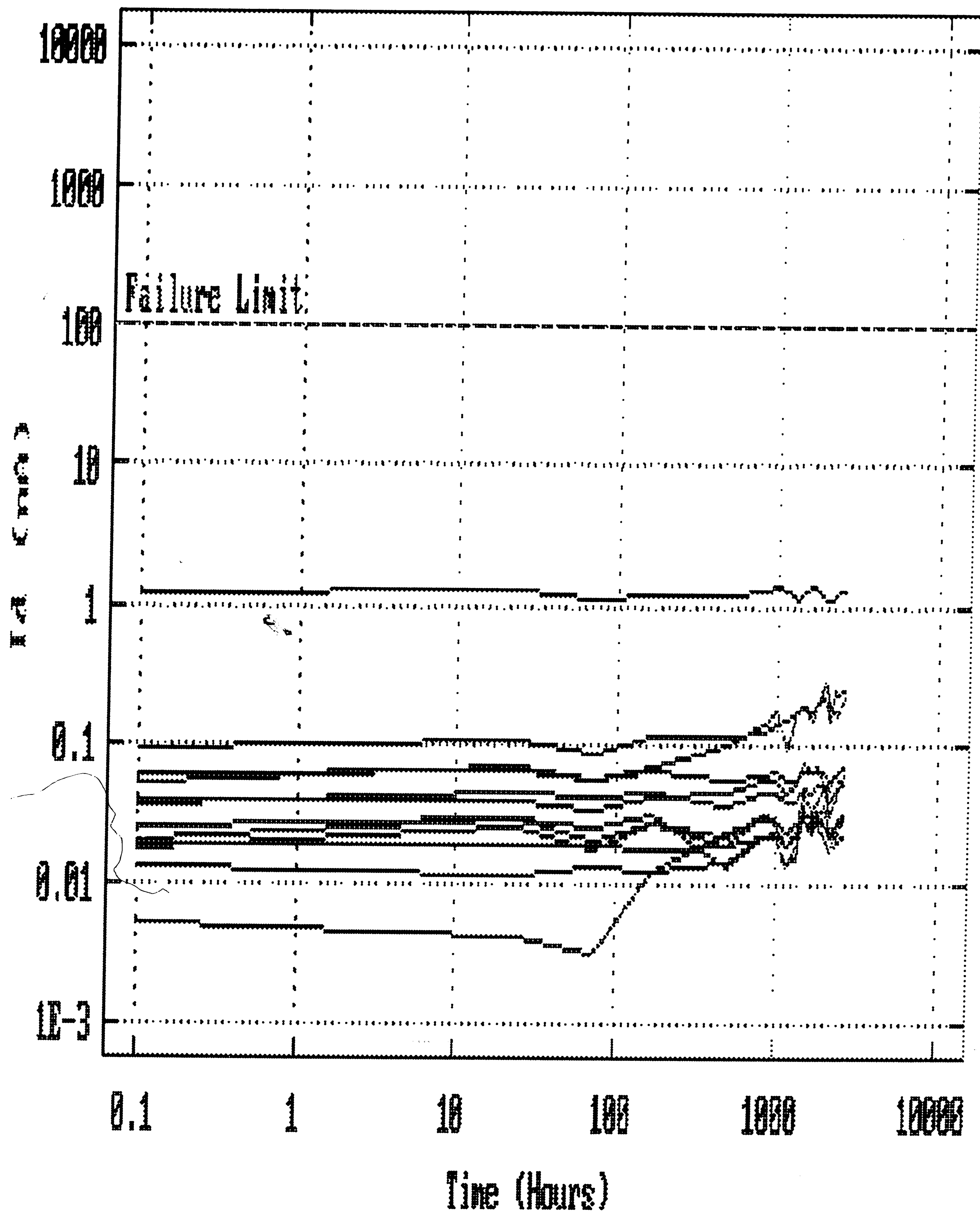

Figure 17(c) Dark Current for 76 μm Diameter Junction Device @ 250 Degree Celsius, Low dI/dV Noise

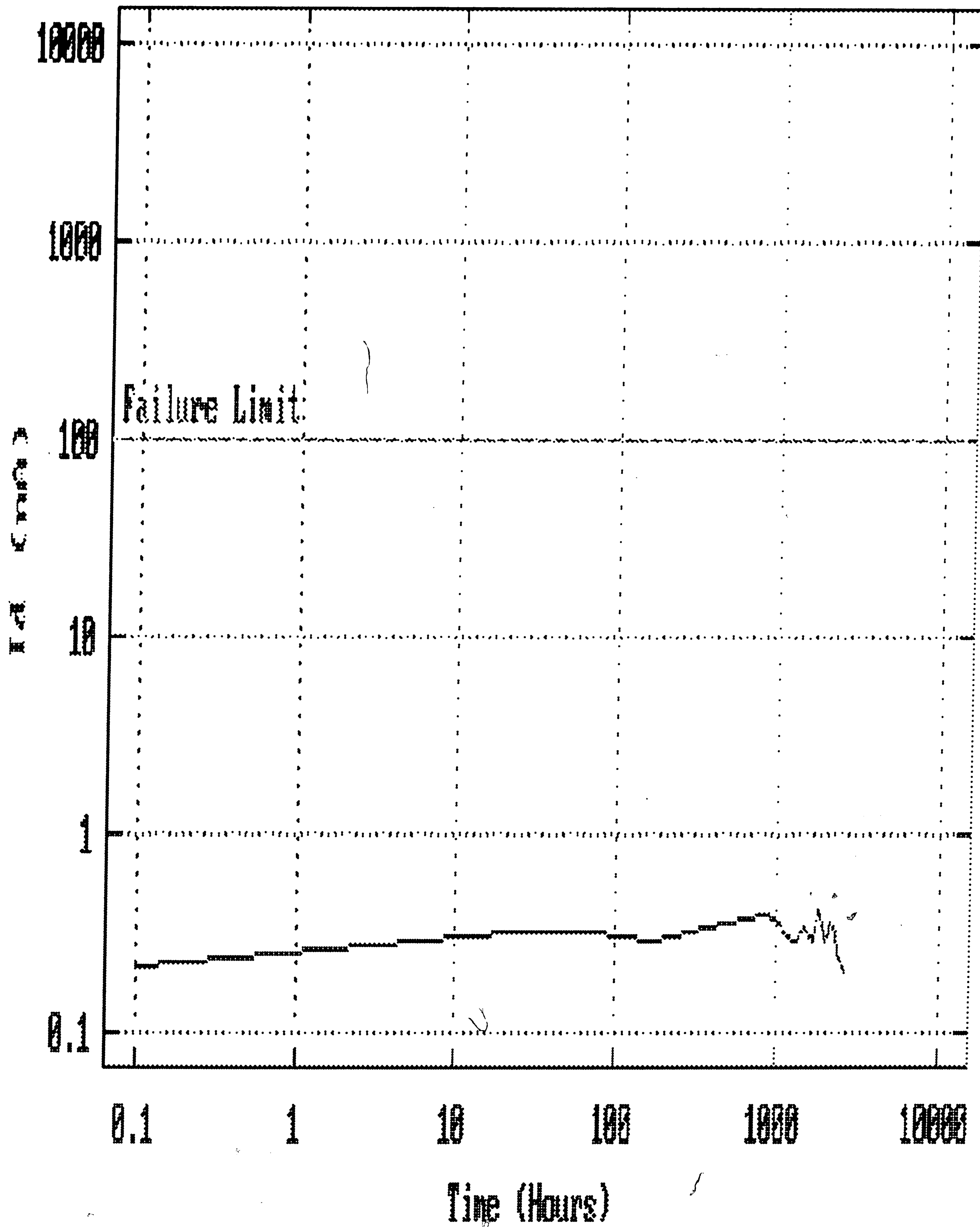

Figure 18(a) Dark Current for 254 μm Diameter Junction Device @ 250 Degree Celsius, High dI/dV Noise

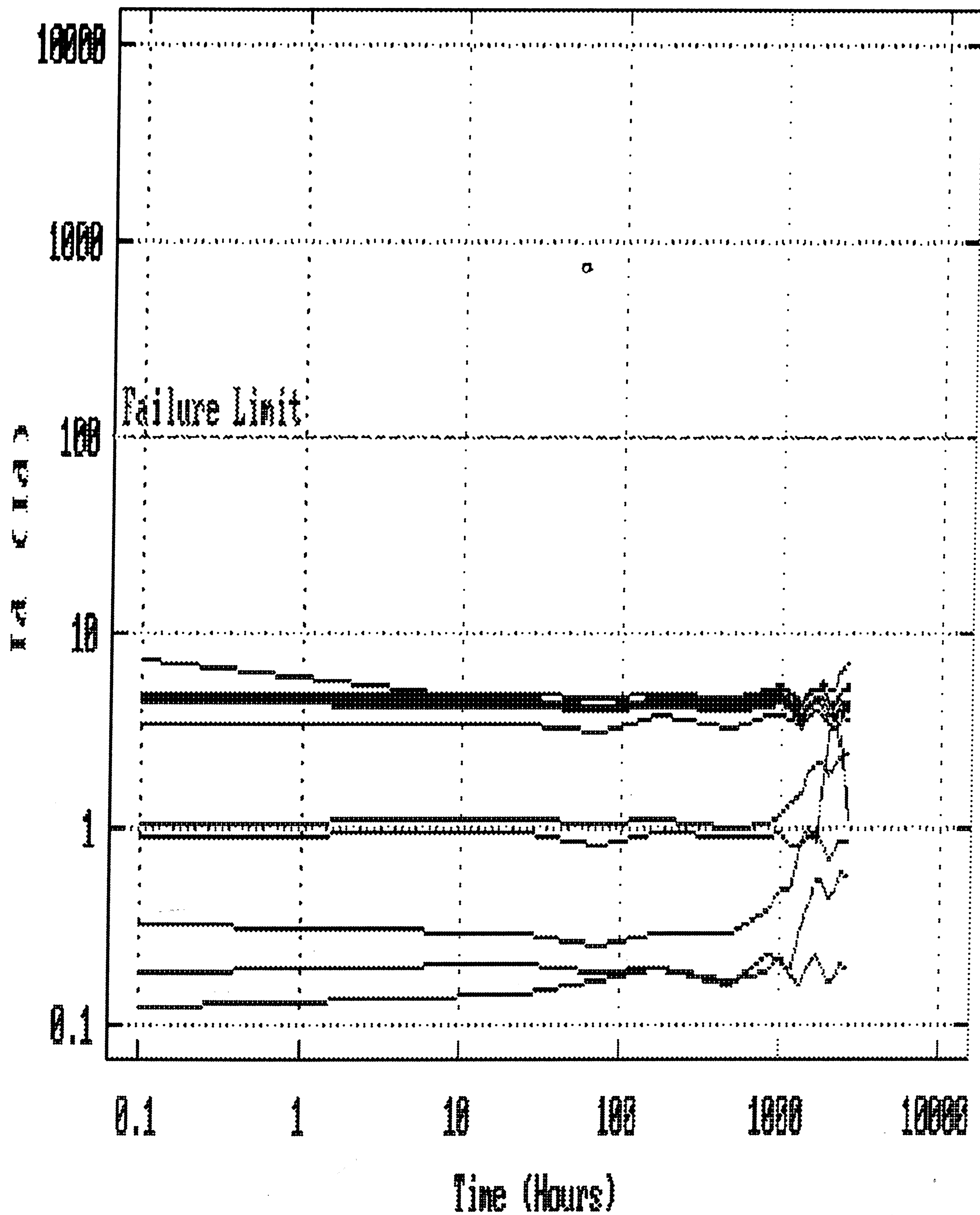

Figure 18(b) Dark Current for 254 μm Diameter Junction Device @ 250 Degree Celsius, Mid dI/dV Noise

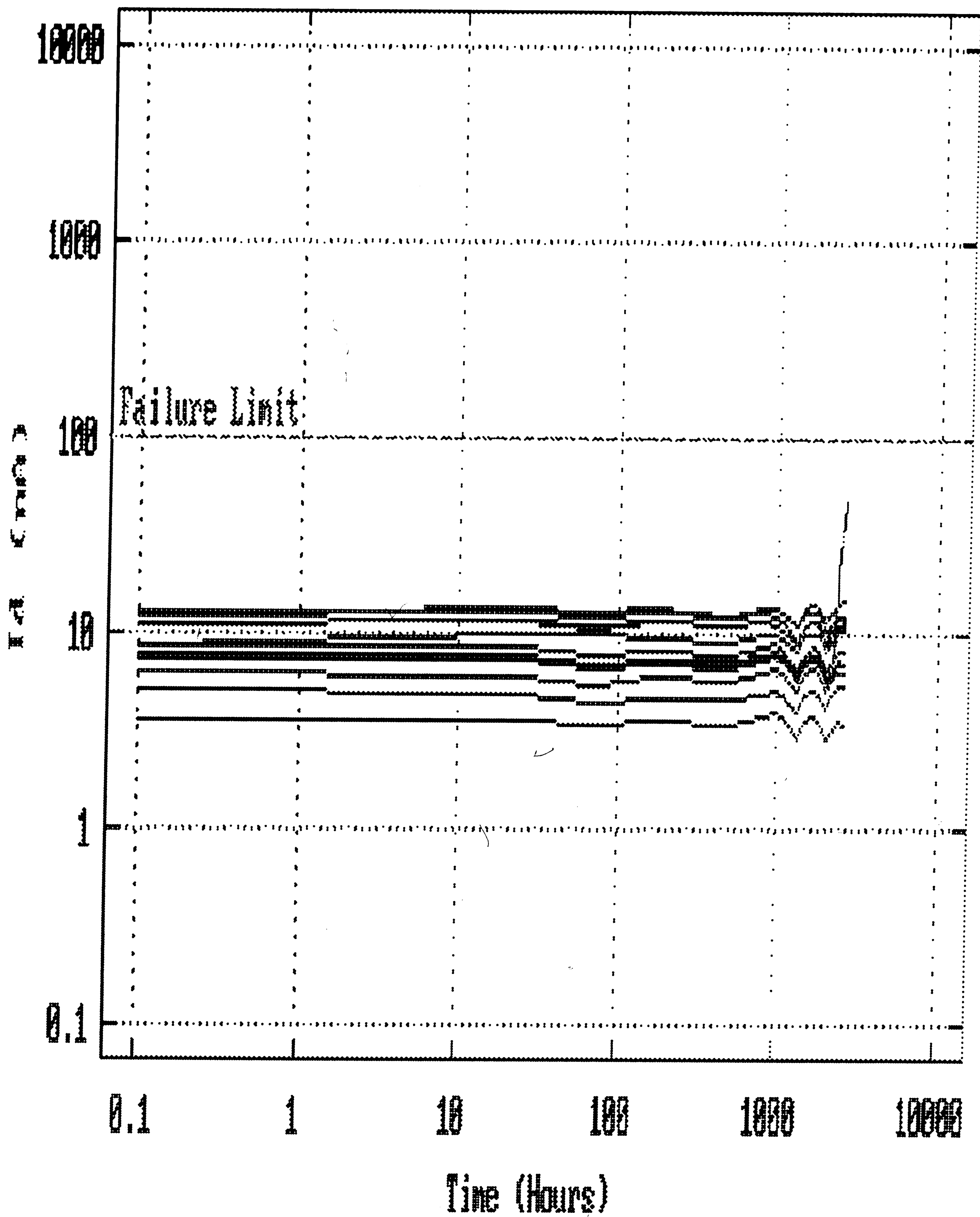

Figure 18(c) Dark Current for 254 μm Diameter Junction Device @ 250 Degree Celsius, Low dI/dV Noise

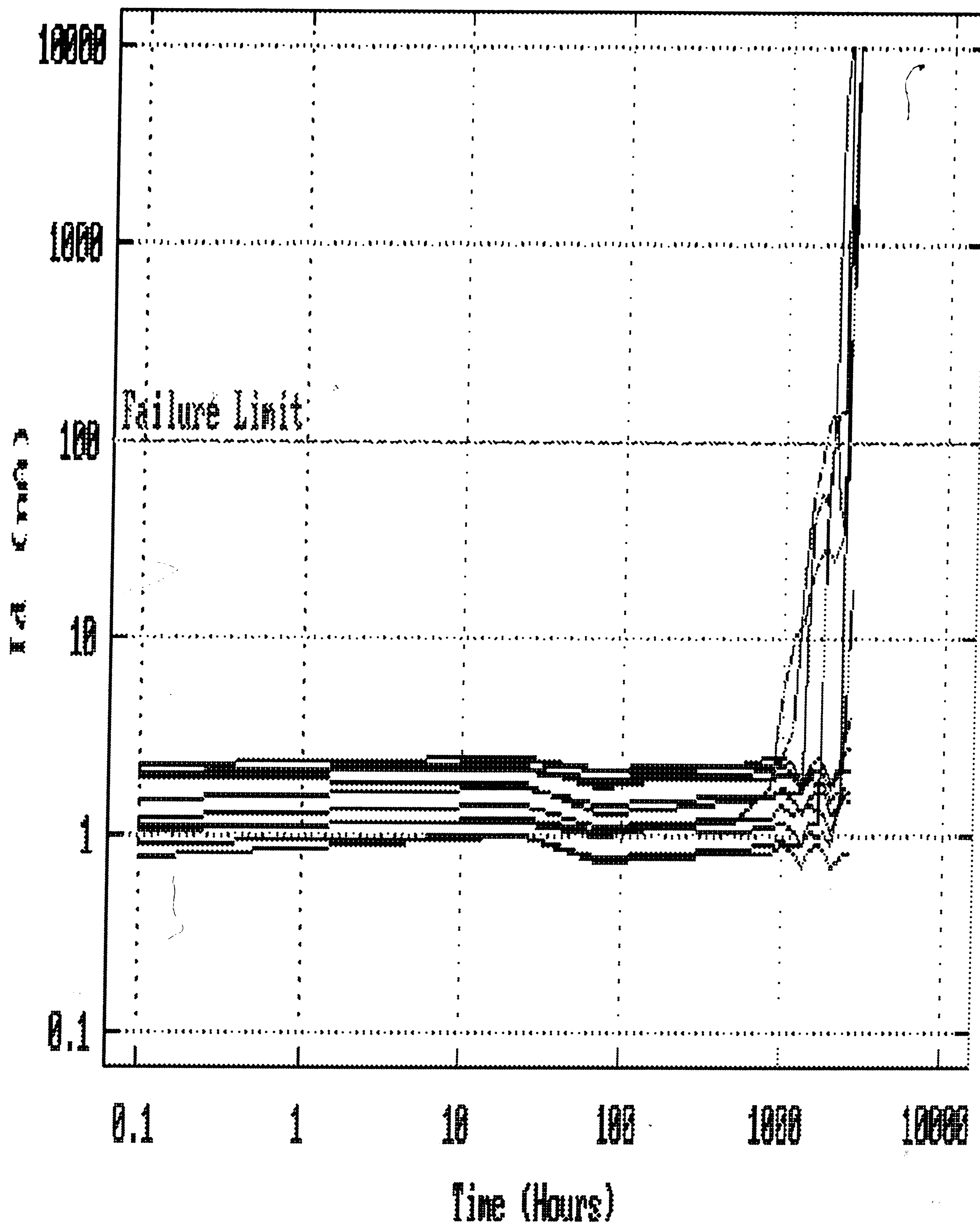

Figure 19(a) Dark Current for 381 μm Diameter Junction Device @ 250 Degree Celsius, High dI/dV Noise

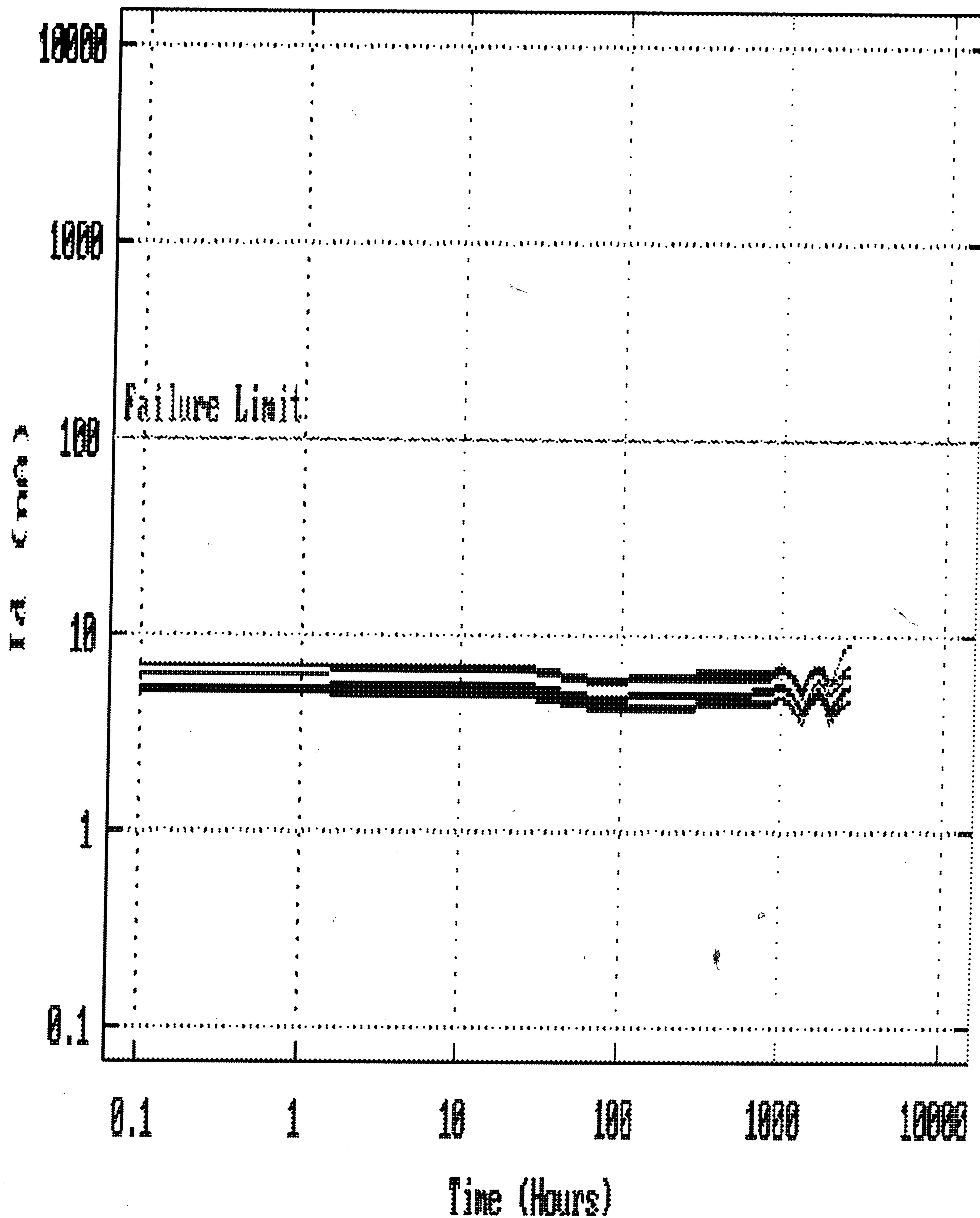

Figure 19(b) Dark Current for 381 μm Diameter Junction Device @ 250 Degree Celsius, High I-V Ratio, Low dI/dV Noise

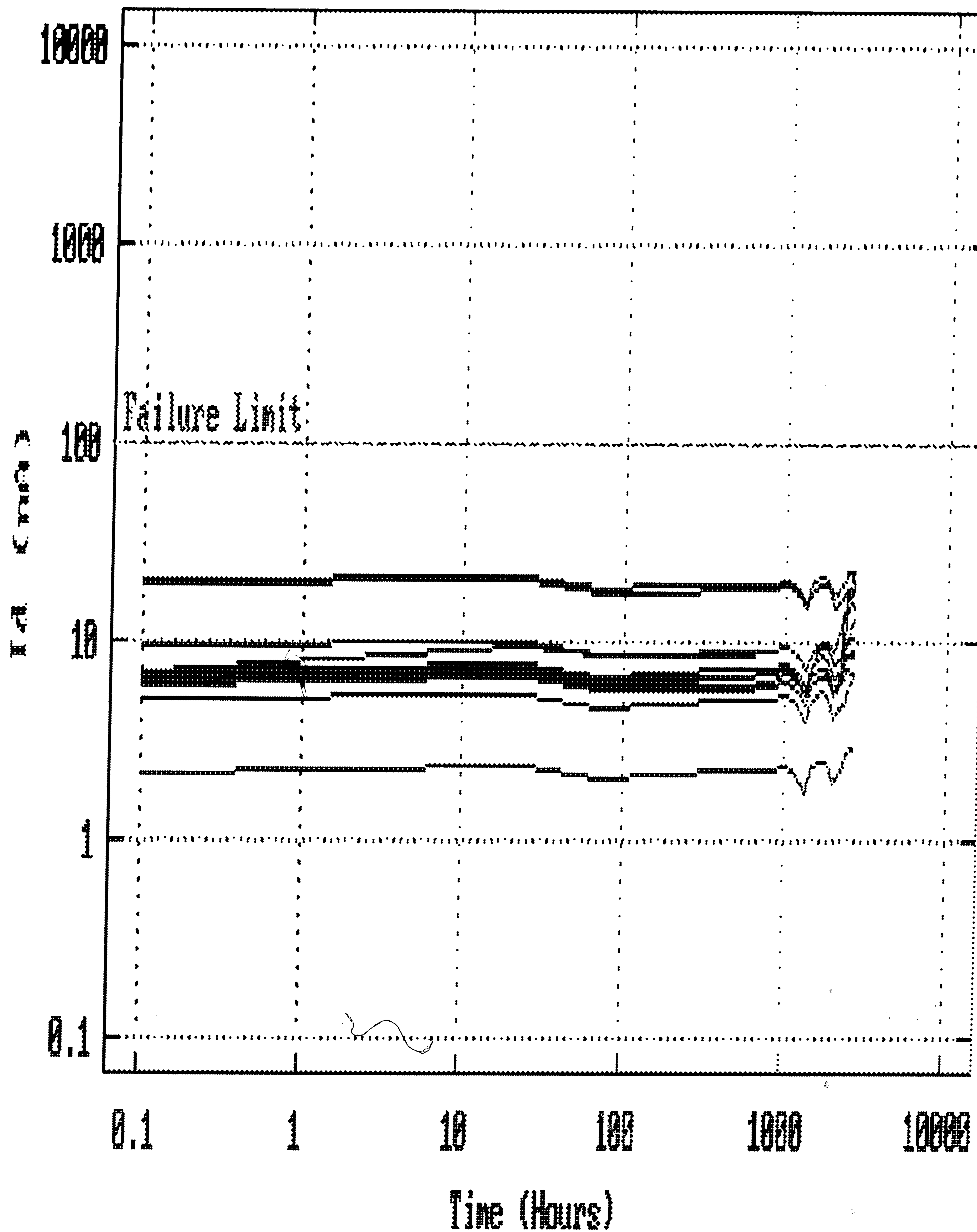

Figure 19(c) Dark Current for 381 μm Diameter Junction Device @ 250 Degree Celsius, Low dI/dV Noise

Reliability Statistics

The cumulative failures for the 250 ^{o}C group are plotted in Figure 20. The slope, ß, for the data is 5.9 suggesting that the failures are wear-out failures, i.e. slope is greater than 1. The activation energy as mentioned earlier is estimated at a worst case value of .6 eV. Using EQ(5) the acceleration factor for 20 ^{o}C service temperature and an aging temperature of 250 ^{o}C is 34,450 (i.e. each hour of accelerated aging is approximately equivalent to 4 years of service operation). The time at which approximately 63.2% of the cumulative failures would occur, η, is extrapolated from figure 20 and is approximately 4200 hours. The predicted MTTF at 20 ^{o}C using a ß=6, η=4200, and the curves in figure 3 is in excess of 10^{13} Hours (>10^{9} years). Using EQ(21) the instantaneous wear-out failure rate is a small fraction of a FIT at 20 ^{o}C.

The were no failures during the 200 ^{o}C aging group. Since no failures occurred, the chi-squared estimation of the FIT rate was used. The value of chi-square for a 90% confidence interval is 4.61 with no failures, see Table 1. Using EQ(5) one can calculate the acceleration factors for different service temperatures for an aging temperature of 200 ^{o}C and a conservative activation energy of .6 eV. With t, time on aging, equal to 4303 hours and N equal to 146 devices (1 ESD failure removed) EQ(19) can be used to calculate the FIT rate at different service temperatures as displayed in Table 7.

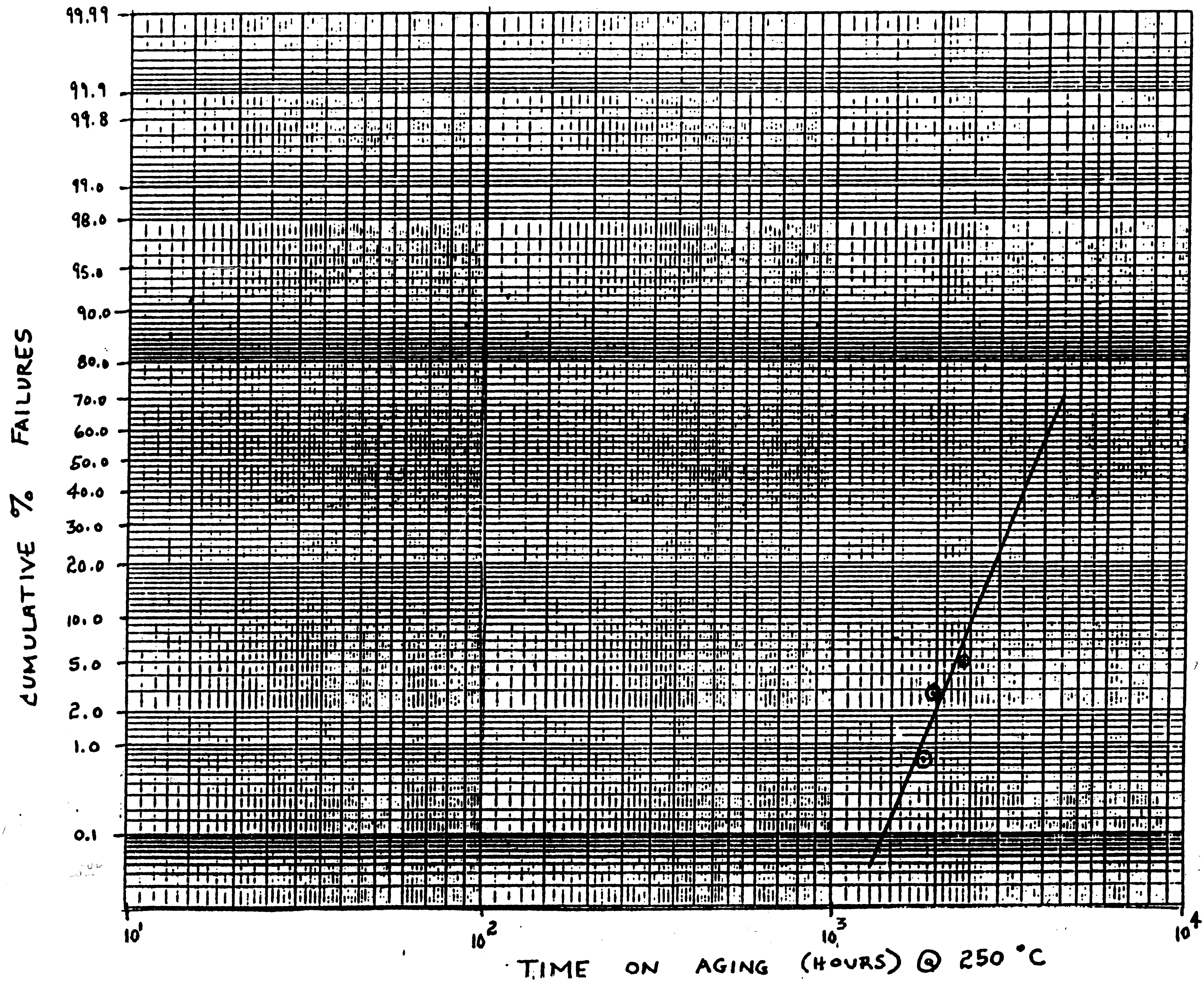

FIGURE 20. CUMULATIVE FAILURE PLOT FOR 250°C CELL

Service Temperature (^{o}C)	Failure Rate (FITs)
10	0.2
20	0.4
40	2
70	14
85	33

Table 7. Predicted Random Failure Rates

The instantaneous wear-out failure rate is dominated by the random failure rate and becomes the failure rate for the device. Since no failures occurred in the 200 ^{o}C group and the activation energy is material/device structure dependent there was no point in calculating the failure rates for different junction size or dI/dV cumulative noise groupings.

The failure rates listed above exceed any current reliability requirements for either terrestrial or submarine applications.

Failure Mode Analysis

Failure mode analysis was performed on all devices which failed the aging study. Two techniques were used to attempt to locate the defect sites: scanning electron microscope (SEM) analysis using an electron-beam induced current (EBIC) signal and chemical etching.

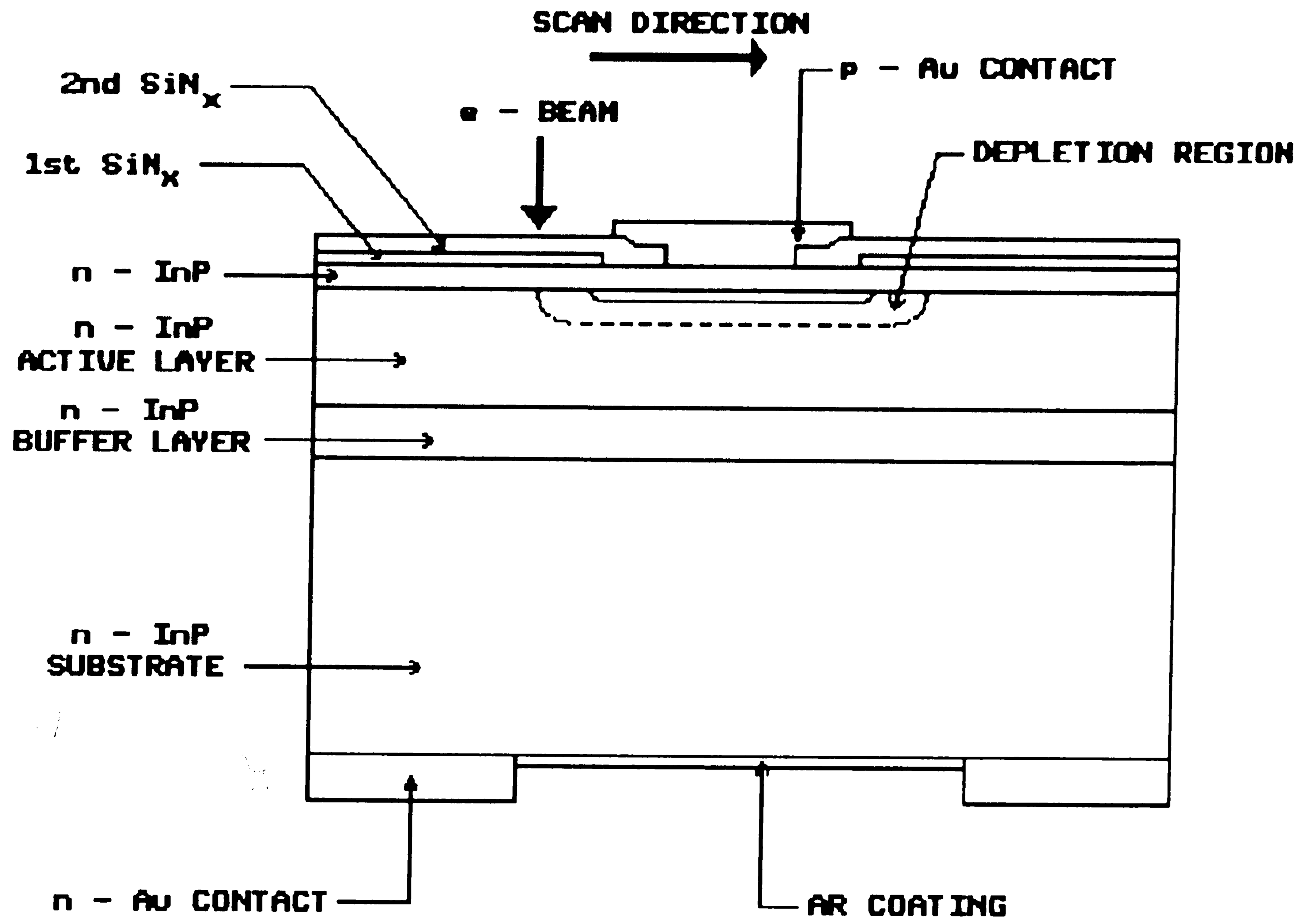

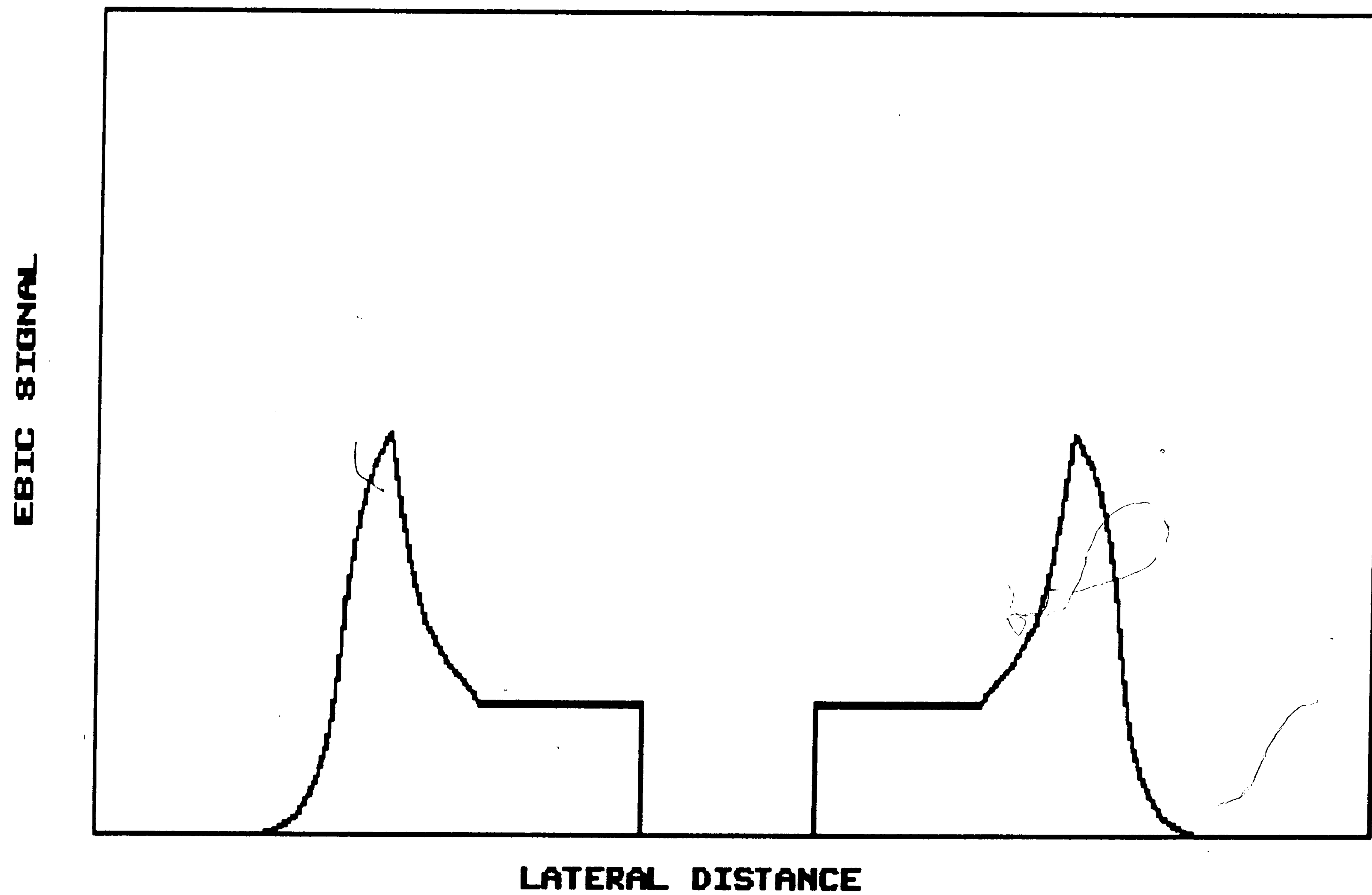

FIGURE 21. SEM schematic using EBIC signal technique

The SEM analysis involves using an electron beam (*e* beam) which is scanned across the *p* region of the diode with the *n* contact bonded down, see Figure 21. As the electrons impinge on the surface of the diode when scanned across the diode an EBIC signal results. The EBIC signal resembles Figure 21 as it is scanned across the diode and is at a maximum where the *p-n* junction comes to the surface of the InGaAs active layer.

As the scan proceeds across the diode surface the signal decreases because of surface recombination and is non-existent when over the contact due to the inability of the *e* beam to penetrate the gold (~1.3um). Figure 22 shows a typical EBIC image.

The EBIC image when compared with a secondary image provides a means of distinguishing between surface particulates and defect sites located under the nitride layers either into the junction region or at its periphery. Because these defect sites are regions of high current density during device operation their presence is enhanced as a "bright" spot in the EBIC image (i.e. more EBIC signal). By increasing the *e* beam strength the intensity of the "bright" spot increases making it easier to identify and also allows for searching for defects deeper in the junction, up to a couple of microns.

The defects which are detectable by the EBIC imaging are attributed to two effects. First, microplasmas which were

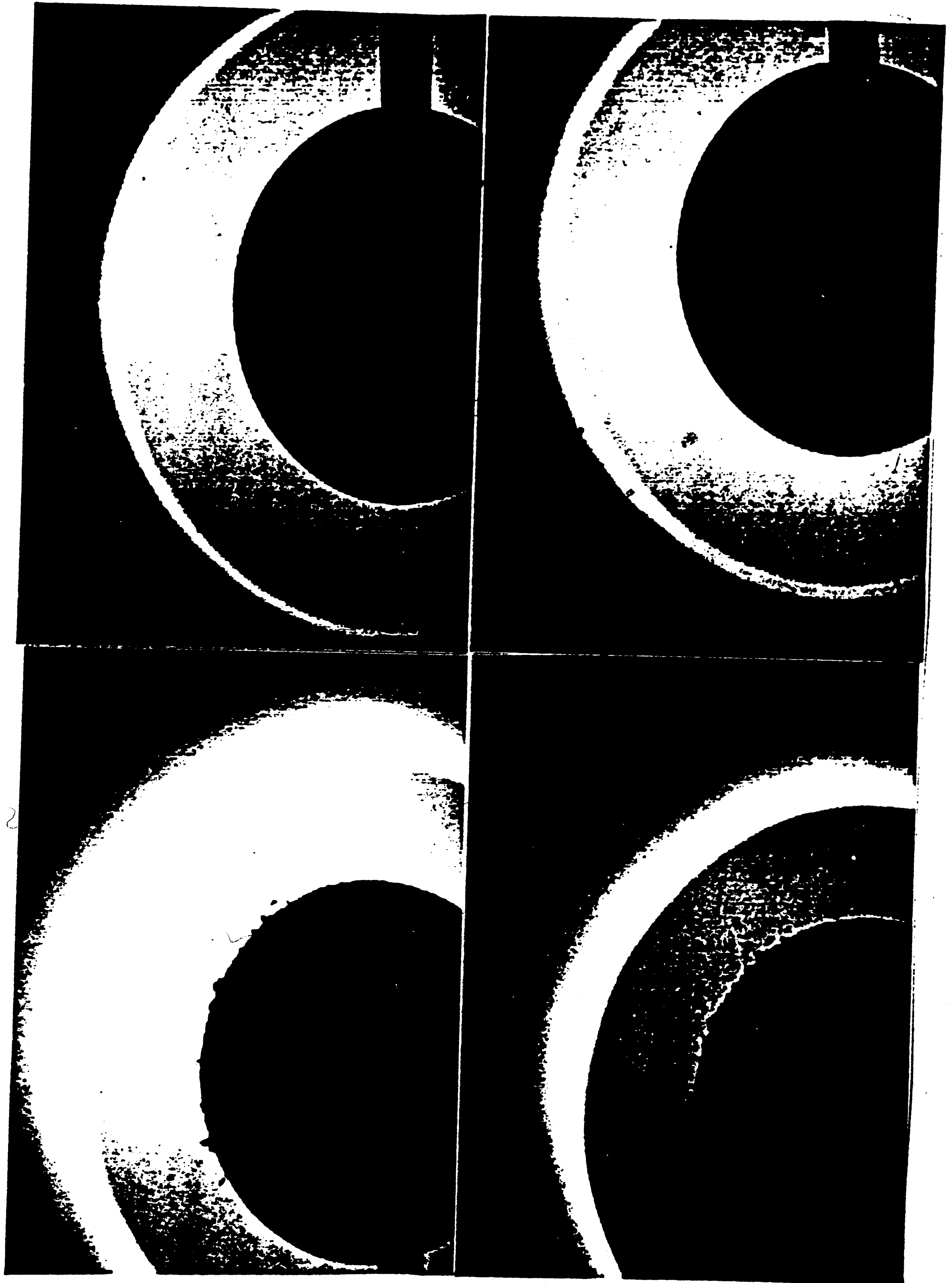

FIGURE 22. EBIC IMAGE OF P-CONTACT FOR A PLANAR PIN PHOTODIODE

created by either pin holes in the surface of the nitride in the case of defects which occurred at the surface of the active region. Second, defect centers which propagated through the epi layers in the form of dislocations or other defects in the substrate material and reside in the bulk of the active region. In depth work was performed by Chin et. al. [20] on these phenomena.

In order to search for defects which are not detectable with SEM because they are located under the Au contact or may be present deep within the junction beyond the penetration capabilities of the *e* beam a chemical etching process can be used. The process consists of removing the different layers of the device using selective chemistry etching in order to observe the device from the *n*-side. First the chips are mounted *p*-side down on a plastic microscope slide using an epoxy resin. The layers are then selectively removed using a chemical etching technique described by M. M. Ecker [29] until the InGaAs active layer is exposed. Pictures are then taken using interference microscopy in areas of suspected damage and then used as a guide when examining the sample under higher magnification. From the *n*-side of the diode the *e* beam is capable of penetrating into the InGaAs into which the junction extends when the photodetector is under bias.

As mentioned earlier, ESD damage is usually visible when using EBIC imaging. Figure 23 shows the "blow-out" that can result from ESD damage. Even though the localized melting is classified as a "blow-out" one can see the magnification required to highlight this phenomena (30KX). It is

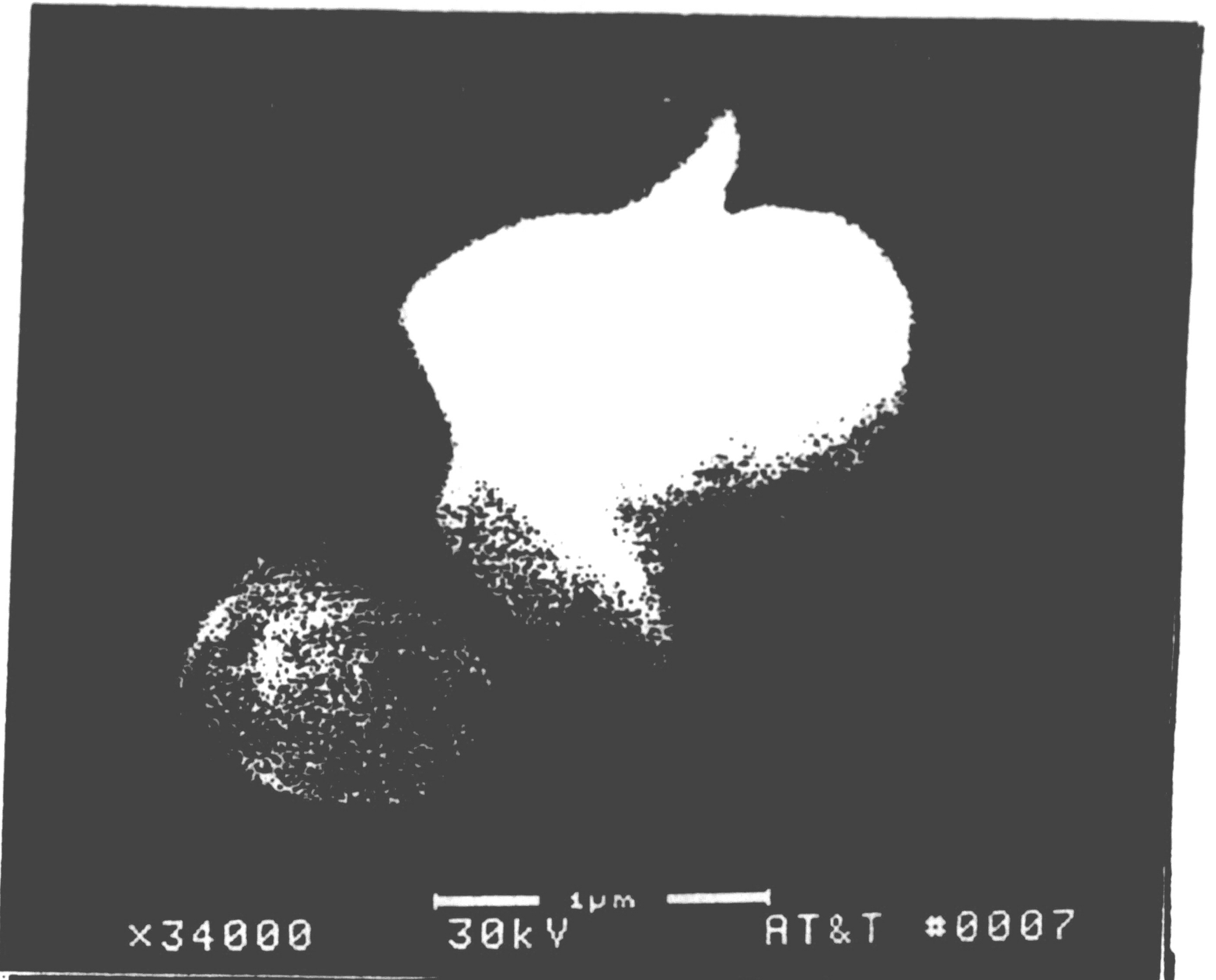

FIGURE 23. SECONDARY IMAGE OF LOCALIZED ESD DAMAGE

extremely difficult to locate these regions unless the damage is severe enough to create a sufficiently large damaged area with respect to the region being examined. The damaged areas in Figures 23 are on the order of 1-3 μm in comparison with a 254 μm diameter junction area. This technique is destructive and was performed after all other non-destructive FMA processes had been completed.

Tables 8 & 9 lists all of the device failures which occurred during aging and the respective failure mode characterized by either FMA technique described earlier. In the case of all 250 ^{o}C failures, the devices were determined to be wear-out failures. There was 1 failure attributed to ESD or other transient damage experienced during the 200 ^{o}C aging process and this device was removed from the population for reliability calculation purposes.

Junc Size (μm)	Wafer	Noise Rating	Aging Failure Mode Delta I_d (nA)
76			
254	165325-387	3.66 (mid)	ESD
381			

Table 8. 200 Degree Celsius Aging Failure FMAs

Junc Size (μm)	Wafer	Noise Rating	Aging Failure Mode Delta I_d (nA)
76			
254			
381	165550-510	2.86 (low)	Wear-out
	165550-515	4.87 (mid)	Wear-out
	165550-518	4.38 (mid)	Wear-out
	165550-524	8.9 (high)	Wear-out
	165550-528	2.81 (low)	Wear-out
	165550-541	6.22 (mid)	Wear-out

Table 9. 250 Degree Celsius Aging Failure FMAs

None of the 250 ^{o}C aging failures showed any noticeable failure modes as seen by Chin et al. using the EBIC imaging with exception of device #541. Figure 24 shows the EBIC image on the top photo, and the bottom two photos are secondary images of the SiN_x surface at different magnifications above the suspect region highlighted in the EBIC image. It seems that some of the nitride that was used as a diffusion barrier when creating the *p-n* junction during the Zn diffusion process was not removed from the junction region creating a undiffused region. This may be a cause of the failure due to the non-uniform fields that are created by the undiffused region. The diode will be submitted to the chemistry lab for further analysis.

All the remaining failures are undergoing further analysis to determine the failure mode and possible cause of failure.

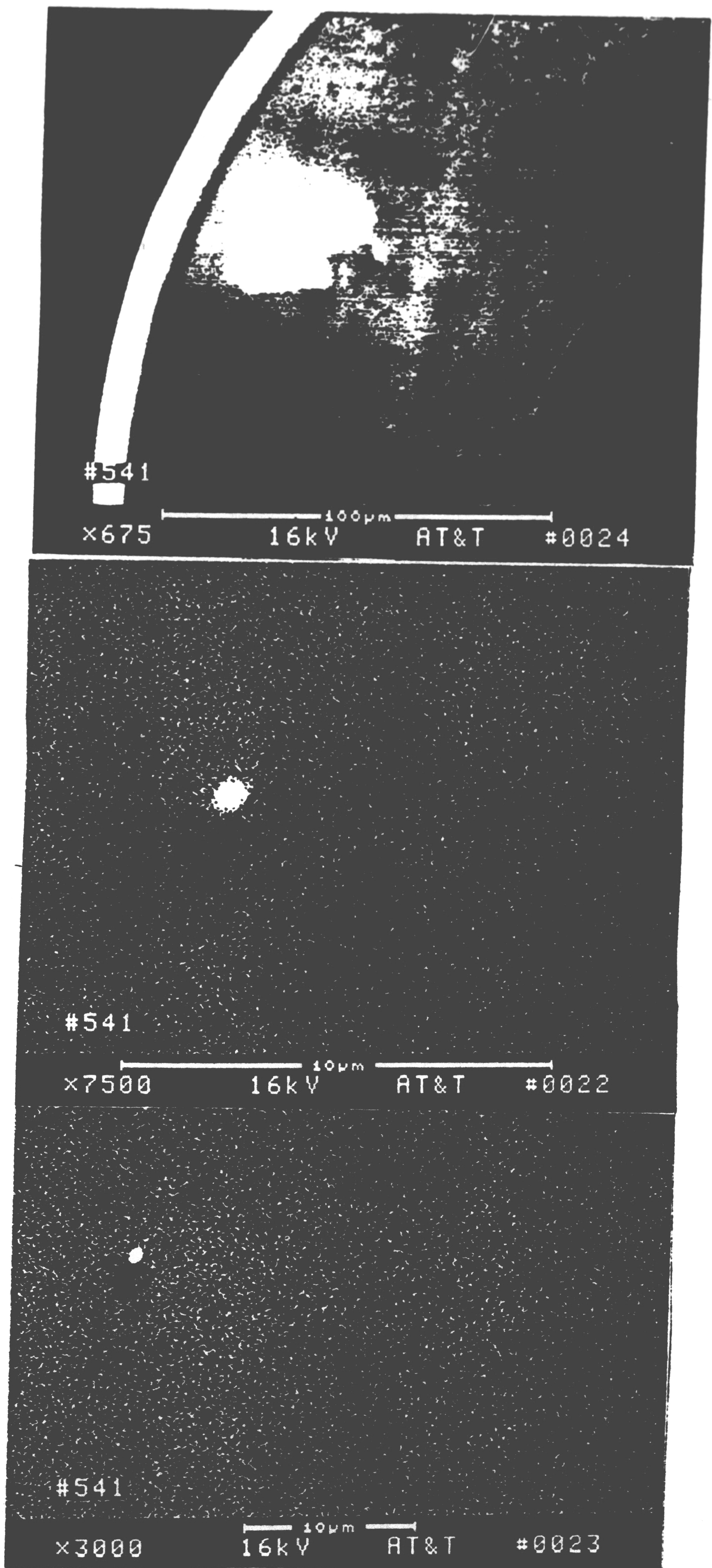

FIGURE 24. EBIC AND SECONDARY IMAGE OF DEVICE # 541

CONCLUSION

The reliability of InGaAs/InP PIN photodetectors manufactured at AT&T are well within the boundaries of current system requirements. Reliability calculations were based on the use of conservative distribution modeling and selection of key parameters such as activation energy to account for the uncertainty in the reliability estimations. These photodetectors exhibited extremely low (< 1) FIT rates and long median lifetimes (> 10^9 years) at room temperature operation and in most cases exceeded the reliability performance of all other photodetectors currently listed in publication. The dI/dV noise measurement developed by Bell Laboratories showed very weak correlation to burn-in as well as aging performance. As a result the noise specifications for all photodetectors are under evaluation and will be relaxed as result of the findings of this study. A significant cost reduction will be realized as a result of specification relaxation. Aging failures did occur in the 250 Degree Celsius group. However, statistical analysis of the data showed the failures to be wear-out failures and are outside of the required service life of device. To date, the work performed in this thesis is the most comprehensive study of reliability for AT&T's long wavelength photodiodes.

REFERENCES

and

BIBLIOGRAPHY

[1] Sutherland, R. R., Skrimshire, C. P., and et al., "A reliability methodology applied to very high reliability planar InGaAs/InP PIN photodiodes" British Telecommunications Technology Journal (1), Vol. 7 (1989), pp. 69-77.

[2] Ripohe, G., Decor, PH., and et al., "First Life-Test Results on Planar p-i-n InGaAs/InP Photodiodes Passivated with SiO_2 or SiN_x+SiO_2 or SiN_x Layers" IEEE Electron Device Letters, Vol. EDL-6 No. 12 (1985), pp. 631-633.

[3] Scholl, F. W., Coden M. H., and et al., "Reliability of Components for Use in Fiber Optic LANs" SPIE Reliability Considerations in Fiber Optic Applications, Vol. 717 (1986), pp. 108-117.

[4] Terauchi, H., Yamaguchi, A., and et al., "InGaAs/InP PIN Photodiode" IOOC-ECOC, Unknown.

[5] Kuhara, Y., Terauchi, H. and Nishizawa, H., "Reliability of InGaAs/InP Long-Wavelength PIN-Photodiodes" IOOC-ECOC (1985), pp. 537-539.

[6] Kuhara, Y., Terauchi, H. and Nishizawa H., "Reliability of InGaAs/InP Long-Wavelength p-i-n Photodiodes Passivated with Polyimide Thin Film" IEEE Journal of Lightwave Technology, Vol. LT-4 No. 7 (1986), pp. 933-937.

[7] Saul, R. H., Chen, F. S., and Shumate P. W., "Reliability of InGaAs Photodiodes for SL Applications" AT&T Technical Journal, Vol. 64 No. 3 (1985), pp. 861-881.

[8] Paul D. K., Greene K. H., and et al., "Undersea Fiber Optic Cable Communications System of the Future: Operational, Reliability and Systems Considerations" IEEE Journal of Lightwave Technology, Vol. LT-2 No. 4 (1984), pp. 414-425.

[9] Li, K. K., and Van Moui, T., "High reliability, all solder construction PINFET receiver using passivated InGaAs PIN photodetector" SPIE Reliability Considerations in Fiber Optic Applications, Vol. 717 (1986), pp. 76-81.

[10] Robertson, and M. J., Ritchie, S., et al., "Highly Reliable Planar GaInAs/InP Photodiodes with high yield made Atmospheric Pressure MOVPE" Electronic Letters, Vol. 24 No. 5 (1988), pp. 252-254.

[11] Ishihara, H., Makita, K., and et al., "High-Temperature Aging Tests on Planar Structure InGaAs/InP PIN Photodiodes with Ti/Pt and Ti/Au Contact" Electronic Letters, Vol. 20 No. 16 (1984), pp. 654-656.

[12] Tashiro, Y., Taguchi, K., and et al., "Degradation Modes in Planar Structure $In_{0.53}Ga_{0.47}As$ Photodetectors" IEEE Journal of Lightwave Technology, Vol. LT-1 No. 1 (1983), pp. 269-272.

[13] Forrest, S. R., Ban, V. S., and et al., "Reliability of Vapor-Grown Planar $In_{0.53}Ga_{0.47}As$/InP p-i-n Photodiodes with very High Failure Activation Energy" IEEE Electron Device Letters, Vol. 9 No. 5 (1988), pp. 217-219.

[14] Saul, R. H., and Chen, F. S., "Reliability Assurance for Devices with a Sudden-Failure Characteristic" IEEE Electron Device Letters, Vol. EDL-4 No. 12 (1983), pp. 467-468.

[15] Bauer, J. G. and Trommer R., "Long-Term Operation of Planar InGaAs/InP p-i-n Photodiodes" IEEE Transactions on Electron Devices, Vol. 35 No. 12 (1988), pp. 2349-2354

[16] Ettenberg, M., and Olsen, G. H., "The Reliability of 1.3 *um* Emitters and Detectors for Fiber Optics" IEEE IEDM (1981), pp. 280-283.

[17] Mabbitt, A. W., Burgess J. W., and et al., "LEDs and PIN FET receivers for long haul fiber optic communication systems" SPIE Fiber Optics: Short-Haul and Long-Haul Measurements and Applications, Vol. 355 (1982), pp. 70-74.

[19] Webb, P.P., and Olsen, G. H., "Large-Area and Visible Response VPE InGaAs Photodiodes" IEEE Transactions on Electron Devices, Vol. ED-30 No.4 (1983), pp. 395-400.

[20] Chin, A. K., Chen F. S., and Ermanis F., "Failure mode analysis of planar zinc-diffused $In_{0.53}Ga_{0.47}As$ *p-i-n* photodiodes" Journal of Applied Physics (6), Vol. 55 (1984), pp. 1596-1606.

[21] Snodgrass, M. L., and Klinman, R., "A High Reliability High Sensitivity Lightwave Receiver for the SL Undersea Lightwave System" IEEE Journal on Selected Areas in Communications, Vol. SAC-2 No. 6, pp. 1008-1014.

[22] Forrest S. R., "Performance of $In_xGa_{1-x}As_yP_{1-y}$ Photodiodes with Dark Current Limited by Diffusion, Generation Recombination, and Tunneling" IEEE Journal of Quantum Electronics, Vol. QE-17 No. 2 (1981), pp. 217-226.

[23] IEEE. Investigation of Microplasmas in InP Avalanche Photodiodes, A reprint from International Electron Devices Meeting December 1979.

[24] Capasso, F., Petroff, P. M., and et al.,"Investigation of Microplasmas in InP Avalanche Photodiodes" IEEE Electron Device Letters, Vol. EDL-1 No. 3 (1980), pp. 27-29.

[25] Magnea, N., Petroff, P. M., and et al., "Microplasma characteristics in InP-$In_{0.53}Ga_{0.47}As$ long wavelength avalanche photodiodes" Applied Physics Letters, Vol. 46 No. 1 (1985), pp. 66-68.

[26] Kim, O. K., Dutt, B. V., and et al., "A Low Dark Current, Planar InGaAs p-i-n Photodiode with a Quaternary InGaAsP Cap Layer" IEEE Journal of Quantum Electronics, Vol. QE-21 No. 2 (1985), pp. 138-143.

[27] Box, G. E. P., Hunter W. G., and Hunter, J. S., Statistics For Experimenters: An Introduction to Design, Data Analysis and Model Building. New York: John Wiley & Sons, 1978.

[28] Keiser, G. Optical Fiber Communications. New York: Mcgraw-Hill Book Co., 1983.

[29] Ecker, M. M., unpublished.

VITA

Mark M. Marvi was born in Knoxville, TN on March 15, 1963 the son of Mr. and Mrs. Nat L. Marvi. He graduated from Pennsylvania State University in 1985 with a Bachelor of Science in Electrical Engineering where he also became certified as an Engineer-In-Training. Currently, he is a Product Engineer with AT&T Microelectronics where he is responsible for technology transfer of new products from development to manufacturing.